



Title	Variations in the terminus position, ice velocity and surface elevation of the Langhovde Glacier, East Antarctica
Author(s)	福田, 武博
Citation	北海道大学. 博士(環境科学) 甲第11345号
Issue Date	2014-03-25
DOI	10.14943/doctoral.k11345
Doc URL	<a href="http://hdl.handle.net/2115/55439">http://hdl.handle.net/2115/55439</a>
Type	theses (doctoral)
File Information	Takehiro_Fukuda.pdf



[Instructions for use](#)

Variations in the terminus position,  
ice velocity and surface elevation  
of the Langhovde Glacier, East Antarctica

FUKUDA Takehiro

Graduate School of Environmental Science  
Hokkaido University



# Contents

<b>Chapter 1</b>	<b>Introduction</b>	5
1.1	The Antarctic ice sheet and its mass budget	5
1.2	Recent changes at Antarctic ice sheet margins	7
1.3	Grounding line	8
1.4	Lack of field data in East Antarctica	9
1.5	Aim of this study	10
<b>Chapter 2</b>	<b>Study site</b>	13
2.1	The Langhovde Glacier	13
2.2	Overview of the study	14
<b>Chapter 3</b>	<b>Field measurements</b>	19
3.1	Methods	19
3.1.1	Hot-water drilling	19
3.1.2	Borehole observations	21
3.1.3	Flow velocity	24
3.1.4	Surface elevation	26
3.1.5	Ice thickness	27
3.1.6	Meteorological observation	29
3.2	Results	30
3.2.1	Hot-water drilling	30
3.2.2	Borehole observations	31
3.2.3	Flow velocity	33
3.2.4	Surface elevation	34
3.2.5	Ice thickness	35
3.2.6	Meteorological observation	36
3.3	Estimation of the bed elevation	37

<b>Chapter 4</b>	<b><i>Satellite image analysis</i></b>	53
4.1	Methods	53
4.1.1	Terminus position	53
4.1.2	Flow velocity	55
4.1.3	Surface elevation	57
4.2	Results	59
4.2.1	Terminus position	59
4.2.2	Flow velocity	60
4.2.3	Surface elevation	61
<b>Chapter 5</b>	<b><i>Discussion</i></b>	71
5.1	Grounding line position	71
5.2	Changes in the terminus position, velocity and surface elevation	74
5.3	Driving mechanism of the changes in the calving rate	76
<b>Chapter 6</b>	<b><i>Conclusions</i></b>	87
	<b><i>Acknowledgements</i></b>	91
	<b><i>References</i></b>	95

# ***Chapter 1 Introduction***

## **1.1 The Antarctic ice sheet and its mass budget**

The Antarctic ice sheet forms the largest ice mass on the earth. The ice sheet covers 98% of the Antarctic continent, which has an area of  $13.924 \times 10^6$  km<sup>2</sup> and a volume of  $26.92 \times 10^6$  km<sup>3</sup> (Fretwell and others, 2013). If the ice sheet melted completely, the meltwater would cause a 58.3 m of sea-level rise (IPCC, 2013). Cogley (2009) and Marzeion and others (2012) revealed that the mean sea level has risen at a rate of  $0.83 \pm 0.37$  mm a<sup>-1</sup> from 2005 to 2009. This rate of sea level rise is greater than the average of the last 3000 years ( $0.1$ – $0.2$  mm a<sup>-1</sup>). It is considered that an acceleration of ice melting is one of the most importance causes of this significant change in the sea level (IPCC, 2013). Most of the glaciers and ice sheets all around the world are losing ice mass under the influence of the warming climate. Contribution of ice melting on the sea level rise is more apparent in mountain glaciers rather than the Antarctic and Greenland ice sheets (Meier and others, 2007). However, if the melting of the Antarctic ice sheet increased, there would be a risk of greater global environmental change because it forms the largest ice on the earth.

The Antarctic ice sheet gains ice and snow-mass from accumulation due to snow fall and condensation in the interior of Antarctica. The accumulated snow metamorphoses into glacial ice by its own weight through densification processes. The ice sheet flows from inland toward the ice sheet margins most rapidly through outlet glaciers and ice streams. These glaciers and ice streams flow faster than the other regions because of enhanced basal ice motion. In the marginal part of the ice sheet, ice forms floating tongues and ice shelves, which are floating on the ocean. The floating tongues and ice shelves are very common structure in the Antarctic coastal regions.

They account for 44 percent of the Antarctic coastline (Drewry, 1983) and their total area is  $1.1 \times 10^6 \text{ km}^2$  (Greve and Blatter, 2009). Processes acting at the interface of the ocean and the ice sheet margins are very important for the ice mass budget of Antarctica, because ablation of ice occurs mostly at floating tongues and ice shelves. The Antarctic ice sheet loses ice mass mostly two important ablation processes: ice berg discharge from fast flowing outlet glaciers and ice streams (calving) and basal melting of ice shelves and floating tongues at the interface with warm ocean water. Ice and snow surface melt in the coastal regions, but its contribution to the total ice mass budget is small as it occurs over a limited area for a short period in summer. Thus, the mass loss process in Antarctica is dominated by the basal melting and calving processes (Depoorter and others, 2013).

Changes in the mass of the Antarctic ice sheet are caused by variations in these accumulation and ablation processes. Because these ablation occurs mostly in the coastal regions, the rate of ice transport from the interior to the marginal region is also plays a role. Thus, studying ice flow is also important to understand the mass change of Antarctic ice sheet. A number of detailed field measurements were carried out and important results are reported from mountain glaciers in the other part of the world, but relatively few field researches have been carried out in Antarctic ice sheet because of its remoteness, harsh environments and logistically difficult conditions. Because of these reasons, studies on the Antarctic ice sheet relies more on remote-sensing techniques. As the remote-sensing technology advances, we can use a wide variety of sensors such as an image camera, a various wavelength band sensors and laser altimeters. Observations by satellite data have made many important achievements in the past, which includes collapse of ice shelves (e.g. Scambos and others, 2004; Cook and Vaughan, 2010), acceleration of ice streams (e.g. Strarns and others, 2008; Lee and others, 2012) and ice thinning along coastal margins of the Antarctic ice sheet.

## 1.2 Recent changes at Antarctic ice sheet margins

Recently, Antarctic ice sheet margins are rapidly changing. One such example is the rapid retreat of Larsen B Ice Shelf in Antarctic Peninsula, observed in 2002 (e.g. Scambos and others, 2004). After the collapse of the ice shelf, thinning and acceleration were observed at outlet glaciers embayed by this ice shelf. Scambos and others (2004) and Rignot and others (2004) reported that the rapid increase in the ice flow velocity and reduction in the surface elevation in the Larsen B Ice Shelf region were caused by the collapse event of the ice shelf in 2002. Similar drastic changes were also observed at other regions of Antarctica. For example, the floating tongue of Thwaites Glacier, Eastern Amundsen Sea was collapsed on a large scale and ice was lost at about 80 km in length in 2002 (MacGregor and others, 2012). From the terminus of the Ninnis Glacier region, East Antarctica, huge icebergs were regularly discharged affecting the ice mass budget in the region (Massom, 2003). And the ice shelves formed over fjord in front of Jones Ice Shelf, Antarctic Peninsula were retreated rapidly from 1998 to 2003 (Fox and Vaughan, 2005).

Another important observation is acceleration of fast flowing outlet glaciers and ice streams. For example, flow velocity has recently increased in the Pine Island Glacier, Eastern Amundsen Sea (Joughin and others, 2003). The velocities of the Pine Island Glacier increased from approximately  $3000 \text{ m a}^{-1}$  during 2003–2005 to  $3500 \text{ m a}^{-1}$  during 2006–2007, to  $4000 \text{ m a}^{-1}$  during 2008–2010 (Lee and others, 2012).

Shephred and others (2001), Wingham and others (2009) and Scott and others (2009) revealed significant changes in the surface elevation of the Pine Island Glacier in the recent years. It is hypothesized that basal melting of ice shelves is increasing because of warming ocean water (Pritchard and others, 2012), resulting in the surface lowering of the glacier. Acceleration and thinning of several outlet glaciers were associated with disintegration of ice shelves in front of the glaciers. Accelerated glaciers

became thinner because they discharged more ice by calving in the ocean. As a result of these changes in the outlet glaciers, the Antarctic ice sheet lost ice mass at a rate of  $-196 \pm 92 \text{ Gt a}^{-1}$  in 2006 (Rignot and others, 2008). Furthermore, the rate of ice mass loss was increasing year by year (Velicogna and others, 2009). Therefore, monitoring front positions, ice flow velocity and surface elevations of fast flowing outlet glaciers is crucial to better understand the current mass loss of Antarctic ice sheet as well as its future evolution.

### 1.3 Grounding line

Antarctic outlet glaciers form floating ice (the ice shelf or the floating tongue) from which the glacier discharges ice into the ocean. The boundary of the floating and grounding ice is called the grounding line. This floating ice is melting at its base at a relatively large melting rate because it contacts with warm sea water (Pritchard and others, 2012). Recent researches reported that the basal melting accounts for 52% of all mass loss through the outlet glacier (Depoorter and others, 2013). Thinning and retreat of an ice shelf causes migration of grounding line upstream and expand the interface of ice and ocean water. This results in further change of the ice shelf under the influence of basal melting. Thus, it is important to understand the location of grounding line for the influence of basal melting and the mass loss of outlet glacier.

Location of the grounding line is hard to determine because subglacial observation is technically difficult. In-situ measurements are not feasible, and thus the location has been identified by using data obtained on the glacier surface. There are two approaches for the estimation of the grounding line position: dynamic and static methods (Brunt and others, 2010). The former approach estimates the position from the vertical motion of ice shelf surface caused by tides. The grounding line is considered as

boundary in a flexural zone from grounded ice to hydrostatically supported ice induced by short term tidal variations within the subglacial cavity (Vaughan and others, 1995). Synthetic Aperture Radar interferometry (InSAR) analysis (Goldstein and others, 1993; Rignot and others, 2011) or ICE-Sat repeat track analysis (Fricker and others, 2006; Brunt and others, 2010) has been used for the measuring the vertical ice motion in the region between grounded ice and ice shelf. The latter approach is based on digital elevation models (DEMs) of ice shelf surface. The images of Moderate Resolution Imaging Spectroradiometer Mosaic of Antarctica (MOA) (Scambos and others, 2007) or Landsat Image Mosaic of Antarctica (LIMA) (Bindschadler and others, 2008) were used to measure the surface elevation for this purpose. The surface topographic features can provide the position of grounding line. The position was highlighted by slope magnitude calculated from the first spatial derivative of the surface elevation data (Horgan and others, 2006).

#### 1.4 Lack of field data in East Antarctica

Contrasting to the numbers of studies using satellite remote sensing techniques, there are relatively few direct evidences of Antarctic glacier changes collected in the field. Because the field research in Antarctica is very difficult due to harsh environments. As compared with the glaciological field research in other regions, for example, European Alps and Alaska region, Antarctic region is a relatively young research field. The research data obtained by the field measurements in Antarctica provide valuable knowledge. Field data are needed to calibrate satellite observations and to establish numerical model simulation, as well as to examine the mechanisms driving the observed changes.

Moreover, most of the detailed researches have been conducted with focus on the outlet glaciers in West Antarctica, for example, the Pine Island Glacier (Scambos

and others, 2004) and Larsen B tributary glaciers: Hektoria, Green, Evans, Punchbowl, Jorum and Crane Glacier (Shuman and others, 2011; Berthier and others, 2012). There are a number of outlet glaciers along the coast of East Antarctica, whose coast line is longer than that of West Antarctica. Monitoring studies on outlet glaciers and ice shelves in East Antarctica are mostly based on satellite observations (Miles and others, 2013). Only a few studies based on the field measurements have been carried out at outlet glaciers in East Antarctica, such as Amery Ice Shelf (Fricker and others, 2002; Yu and others, 2010) and the Byrd Glacier (Stearns and others, 2008).

## 1.5 Aim of this study

To better understand the mechanism driving recent changes of outlet glaciers in East Antarctica, we carried out detailed studies on the Langhovde Glacier. This glacier is located on the Soya Coast nearby the Japanese Antarctic research base, Syowa Station. Special focus of our study was the changes in terminus position, ice flow velocity and surface elevation, and their connection with surrounding environments, such as air temperature and sea ice conditions. We combine satellite-based and field observational data to investigate recent changes occurring at the Langhovde Glacier. We performed field measurements to obtain ice flow and ice thickness near the terminus of the glacier as a part of the 53rd Japanese Antarctic Research Expedition (JARE 53). These field data were compared with those obtained by satellite image analysis to quantify the changes over the last decade. We studied this glacier because of the feasibility of field activity on the glacier. Outlet glaciers are usually very difficult to work as they are covered with many crevasses. The Langhovde Glacier has relatively flat surface, which enabled us to carry out various field observations in the field. In this study, the changes in the terminus position, flow velocity and surface elevation of the Langhovde Glacier were quantified for the period from 2000 to 2012.

Our data shows that this glacier is in a relatively stable condition over the study period. The data also demonstrate the importance of sporadic calving events in frontal variations. Furthermore, the sea ice formed in front of the glacier is considered as a possible reason of the variations in the calving rate. These results contribute to better understanding of variations and ice dynamics of outlet glaciers in East Antarctica.



## ***Chapter 2 Study site***

### **2.1 The Langhovde Glacier**

The Langhovde Glacier (69°11'S, 39°32'E) is located on the Soya Coast at about 20 km south of Syowa Station in East Ongul Island, a Japanese Antarctic Research Expedition (JARE) base (Fig. 2-1). There is 600-m-deep glacial trough in front of the glacier. The deep trough lie along margin of continental ice sheets to Ongul Strait located between East Ongul Island and the ice sheets (Fujiwara, 1971). The glacier flows into the Lützow-Holm Bay, through a 3 km-wide calving front. The fast flowing region is extending inland from the calving front for about 10 km. Ice surface is fairly flat in the lower few kilometers, suggesting the formation of a floating tongue in this region. The glacier is bound by relatively slowly moving ice to the east and bedrock to the west. The glacier flows faster than the surrounding ice at a rate more than 100 m a<sup>-1</sup> and discharges ice into the ocean by calving.

Since JARE began its activity in 1956, a variety of research work has been performed in the studied region. Particularly in the region nearby the Langhovde Glacier, a number of field studies have been carried out in many different scientific fields, i.e. geology (e.g. Matsumoto and others, 1979), geomorphology (e.g. Sawagaki and others, 2008), geophysics (e.g. Kamimura and Shibuya, 1983; Nogi and others, 2013), oceanography (e.g. Harada and others, 1995; Ohshima and others, 1996; Kawamura and others, 1997; Aoki and others, 2000), climatology (e.g. Ohtani and others, 1990) and biology (e.g. Kanda, 1986; Kudoh and others, 2009). In contrast to the variety of research activities performed on land, ocean and lakes, only a few field activities have been conducted on the Langhovde Glacier. Aircraft observations were conducted a number of times in 1962–1991 to take aerial photographs to generate maps (Komazawa

and others, 2013). A glaciological research was carried out in 1999/2000 at the upstream region of the glacier as a part of the JARE 41st summer activity. In this research project, mass balance measurements with snow stakes, flow velocity measurement using Global Positioning System (GPS) and radar sounding for measuring ice thickness were performed (Nishimura and Pattyn, personal communication).

## 2.2 Overview of the study

In this study, we carried out field measurements as a part of the JARE 53rd summer activity. The expedition team left West Australia for Antarctica by an icebreaker “Shirase” on 30th November, 2011. The ship traveled southward across the Indian Ocean along a 110 degrees east longitude with several stops for oceanographic observations. At the latitude of 60 degrees south, the ship turned to the eastward for Syowa Station. We reached the northern margin of the fast ice region on 17th December and started to break sea ice to approach the station. Unfortunately, ice was too thick to break in this season, so that the cruise was delayed. Ice near Syowa Station was thicker than ever observed in this region, presumably because of superimposed ice formation due to heavy snowfall on the fast ice (Ushio, 2012).

For the activity on the Langhovde Glacier, we left the ice breaker on 28 December by a helicopter for a research hut at Yukidori-sawa located 6 km southwest of the glacier. All research equipment was transported to the hut by a helicopter operated by Shirase. We established a camp in the vicinity of the glacier to carry out a reconnaissance survey to find places suitable for drilling and measurements on the glacier. A reference GPS station was installed at the peak of a bedrock hill during this reconnaissance activity (see chapter 3.1.3.). We decided to establish our camp at Site 1 (see Fig. 2-1 for location), where we drilled first two boreholes. All equipment required

for measurements, drilling and camping were transported to Site 1 by a middle-sized helicopter operated by JARE on 2nd January, 2012. The camp was moved with the equipment on 15th January to the second drilling site (Site 2) located about 500 m upstream from Site 1. Two more boreholes were drilled and other glaciological measurements (GPS measurements and radar soundings) were performed during our stay at Site 2. After the hot water drilling was completed, we dismantled the camp and transported the equipment from the Langhovde Glacier to Syowa Station on 29th January. Some of field activities were continued until 9th February, by using helicopter transport from Syowa Station.

Locations of our field measurements are shown on a map in Fig. 2-1. Four boreholes were drilled with a hot-water drilling system at BH1 and BH2 at Site 1, and BH3 and BH4 at Site 2. Various observations (borehole camera, water pressure and oceanographic observations) were conducted using these boreholes to measure physical properties in the subglacial environment. Glacier flow, surface elevations and ice thickness measurements were carried out on the glacier surface. We operated GPS receivers continuously to perform high frequency ice flow velocity measurements at GPS1–4. These GPS measurements require a fixed reference GPS station, which we established outside of the glacier at GPS FIX as indicated in Fig. 2-1. Surface elevation and ice thickness were measured over the glacier within 0.3–3.5 km from the terminus. During the field measurements, climatic observation was performed near Site 1 (AWS in Fig. 2-1). Coordinates of these measurement sites are listed in Table 2-1.

Satellite image analyses were performed for the glacier terminus position, flow velocity and surface elevation over a period of between 2000 and 2012. The analyzed images which have an area of 6 km × 6 km square were cropped from various kinds of satellite images. These images covered the terminus region in the lower 5 km of glacier

including slow flowing Antarctic ice sheet and fixed bedrock. Data from bedrock area was used to setup ground control points (GCP) to adjust images and to calibrate flow velocity analysis.

Table 2-1 Coordinates and elevation of the measurement points.

Measurements	Name	Latitude	Longitude	Elevation(m)
Hot-water drilling	BH1 (Site1)	69°12'08.67"S	39°49'21.12"E	40.8
	BH2 (Site1)	69°12'08.72"S	39°49'20.80"E	40.8
	BH3 (Site2)	69°12'24.22"S	39°49'26.63"E	52.9
	BH4 (Site2)	69°12'24.25"S	39°49'25.81"E	52.6
GPS	GPS FIX	69°12'49.17"S	39°44'39.88"E	47.6
Velocity	GPS1	69°11'03.46"S	39°47'01.61"E	20.3
	GPS2	69°11'37.06"S	39°47'51.44"E	31.9
	GPS3	69°12'10.33"S	39°49'22.87"E	42.8
	GPS4	69°12'23.28"S	39°49'33.84"E	55.9
Elevation		69°11'04.09"S	39°46'34.22"E	22.2 – 58.8
		-69°12'47.63"S	-39°49'58.72"E	
Ice Thickness	IR1-5	69°11'15.62"S	39°46'34.22"E	26.7 – 58.8
		-69°12'47.63"S	-39°49'42.26"E	
Local weather	AWS	69°12'13.15"S	39°49'13.67"E	51.1

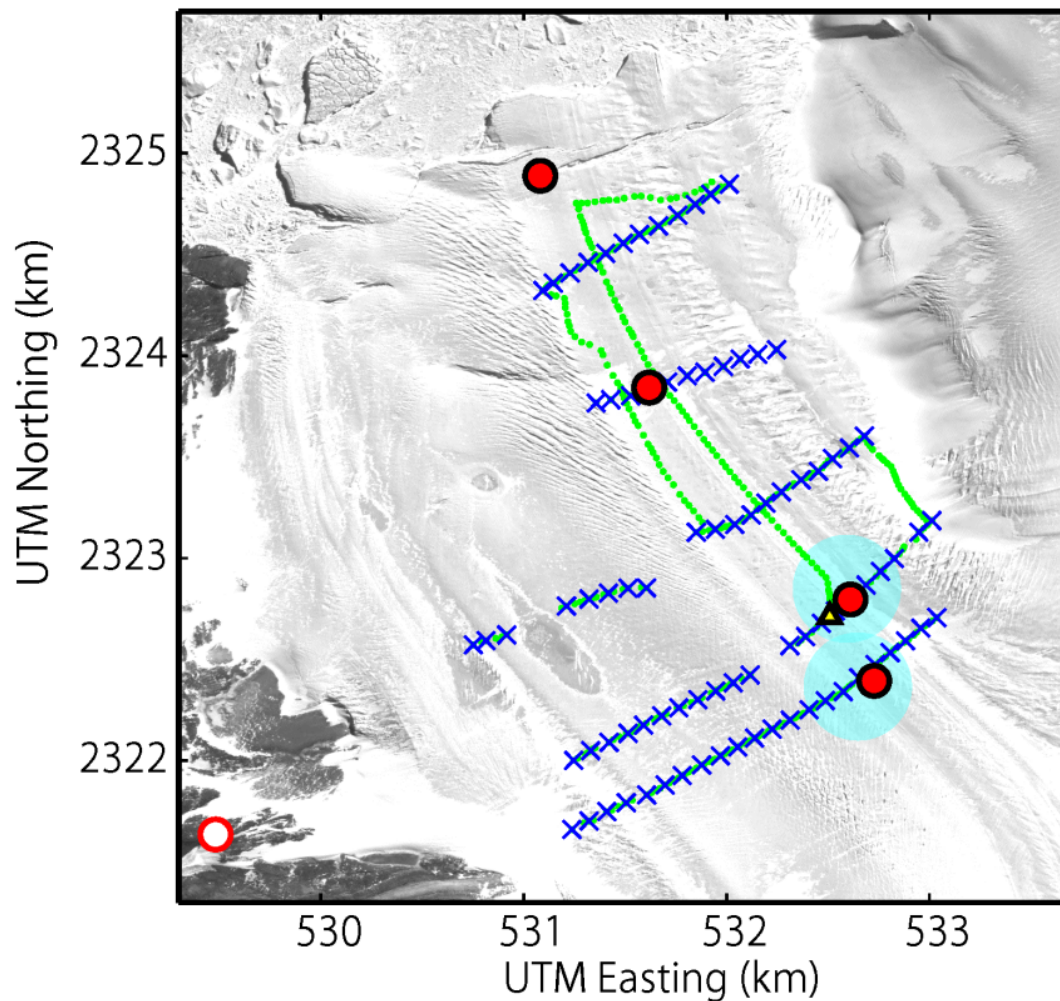


Fig. 2-1 Satellite image showing the locations of the field activities in the terminus part of the Langhovde Glacier. The hot-water drilling sites (Site 1, 2) are shown by the areas shaded in cyan. GPS measurement station (GPS14) and reference station (GPS FIX), survey points of the surface elevation and ice thickness are indicated by red and open circles, green dots and blue crosses, respectively. The background is an ALOS/PRISM image taken on 10th October, 2010.

## ***Chapter 3    Field measurements***

### **3.1    Methods**

#### **3.1.1    Hot-water drilling**

Hot-water drilling was performed in two regions, Site 1 and Site 2 (Fig. 2-1). They were located at 2.8 km and 3.3 km from the terminus, respectively. We used a hot-water drilling system developed in the Institute of Low Temperature Science (ILTS), Hokkaido University (Fig. 3-1). The key instruments of the system are three high-pressure hot-water machines, HDS1000BE (Kärcher GmbH & Co. KG). Each of the machines consists of a water pump driven by a petrole-fueled reciprocal engine (Honda, GX390), and a diesel oil burning coiled pipe heating system. This system is able to produce hot-water at a rate of 15 L min<sup>-1</sup> at about 80 °C (Tsutaki and others, 2009). In addition to the hot-water system, our drilling system uses hundreds meters of high pressure and heat-resistance hoses (we used 100, 75 and 50 m long hoses connected by couplers) and a winch driven by hand and electricity for hanging the hose in a borehole. We also used a pulley and tripod instead of the winch when we drilled shallow (< 100 m) boreholes. At the end of the hoses, a 3.2 meters long stainless metal pipe (outer diameter 34 mm, weight 13.7 kg) manufactured in a workshop of ILTS with a commercially available jet nozzle (2.0 mm in diameter) (Type K-20, Katorigumi Seisakusho Ltd.) were connected to spray hot-water jet. Our drilling system has been used at mountain glaciers in other regions. The first version of the system was used for drilling a total length of about 3000 m in Rhonegletscher in the Swiss Alps in 2007–2009 (Sugiyama and others, 2008; Tsutaki and others, 2011; 2013). The system was updated later to drill boreholes with greater depths (> 500 m), and used at Glaciar Perito Moreno, in the Patagonia Ice Field in 2010 (Sugiyama and others, 2010; 2011).

Drilling full depth of the Langhovde Glacier requires greater amount of heat supply than that at the other glaciers mentioned above, because glacier ice is expected to be cold and approximately 400–500-m thick. These estimations were based on annual air temperature measured at Syowa Station and surface elevation above sea level at the floating part of the glacier which was measured by a DEM analysis (see chapter 4.3). For this reason, we employed three of the high-pressure hot-water machines for our drilling campaign at the Langhovde Glacier. To increase the flow rate of hot water, two of the hot-water machines were connected in parallel. Outflow from these two machines was lead to the heater of the third hot-water machine to have a greater temperature. As a result, the system produces hot-water jet of about 85 °C at a rate of 30 L min<sup>-1</sup>.

The drilling operations were carried out on 6th and 8th January, 2012 at Site 1, and on 16th and 21st January at the Site 2 (Fig. 2-1). Water was pumped up from glacier melt water stream running on the ice surface (Fig. 3-1). During the drilling, the hoses and jet nozzle were lowered down into a borehole approximately at a uniform rate (less than 1 m min<sup>-1</sup>). The drilling rate was progressively reduced as the borehole depth increases. Drilling at an adequate and uniform rate is important to excavate a vertical borehole with a uniform diameter. Too fast drilling results in leaning of the jet from the vertical direction, whereas slower drilling requires unnecessary greater amount of fuel. We confirmed that the drilling hoses and nozzle were hung straight down through a borehole, by weighing the hose from time to time. Leaning of the hoses to a borehole wall results in a reduction of the load measured on the surface (Sugiyama and others, 2010). This procedure is also useful to recognize when the nozzle reaches the bed of the glacier.

### 3.1.2 Borehole observations

Subglacial and englacial environments were investigated by using various observational instruments inserted into the boreholes after the hot-water drilling. Here, we describe the details of instruments and procedures employed for the borehole observations.

- Borehole camera

For visual observations within the boreholes, in the subshelf water layer, and at the seabed, two types of borehole video cameras; a bio-logging camera (Little Leonardo Ltd.) and a wearable Bluetooth camera LX2 (Looxcie Inc.) were used in this study. The bio-logging camera was designed for the use at >500 m water depth. The camera was combined with an illumination housing (52 mm in diameter), which was equipped with super luminosity white LED chips. Because the wearable camera was not pressure proof, it was enclosed in a high water pressure (5 MPa) metal container (60 mm in diameter) with LED illumination.

We carried out borehole camera observations immediately after the hot-water drilling, and repeated the observations several times in each borehole. These observations were carried out on 6th, 9th–10th, 16th–17th and 21st January at BH1–4, respectively. When they were operated, cameras were lowered into the boreholes at a rate of about  $1 \text{ m s}^{-1}$ , using a 3 mm diameter Kevlar fiber rope. The depth of images was recorded with a pressure sensor attached to the rope. These cameras were not remotely monitored nor controlled. Recorded video data were stored in a memory device contained in the camera, and recovered after a few hours of measurements when they were retrieved out of the boreholes. The captured movies were played and examined on a computer.

- CTD profiler

Water salinity and temperature in the borehole and beneath the glacier bottom were measured by a CTD (conductivity, temperature and depth) profiler: Ocean Seven 304 Plus (IDRONAUT S.r.l.). We used this profiler because it is thin (43 mm in diameter) enough to lower down through the borehole to the bottom. This instrument records water conductivity with an accuracy of  $3 \mu\text{s cm}^{-1}$  and this conductivity was converted into salinity by using an equation;

$$S = -0.08996 + 28.292972 R_{15} + 12.80832 R_{15}^2 - 10.67869 R_{15}^3 + 5.98624 R_{15}^4 - 1.32311 R_{15}^5 \quad (\text{eq. 3-1})$$

$$R_{15} = C(s, 15, 0) / C(35,15,0) \quad (\text{eq. 3-2})$$

where  $S$  is the salinity (‰),  $C(s,15,0)$  is the conductivity of the sea-water at 15 °C and atmospheric pressure and  $C(35,15,0)$  is the conductivity of standard “Copenhagen” sea water (Lewis, 1980). Water temperature was measured with an accuracy of 0.005 °C. Accuracy of water pressure measurement was 0.5 Pa (0.05 % of full scale).

The measurements were carried out at BH2 on 9th January and BH3 on 17th and 18th January. The CTD profiler was fixed to the Kevlar fiber rope and inserted into the borehole at a rate of about  $1 \text{ m s}^{-1}$ . While the sensor was lowered from the water surface to the seabed, salinity, temperature and depth data were recorded on an internal flash memory with 0.1 second intervals. After the measurement, the obtained data were downloaded and processed by a computer.

- Water Pressure

After the borehole video camera and CTD observations, a water pressure sensor was installed in the subshelf cavity to measure variations of the water level in the boreholes. In this study, we used piezometer 4500SH (Geokon, Inc.) (25 mm in diameter), which measures hydrostatic pressure using a vibrating wire. The accuracy of the sensor was within  $\pm 0.1\%$  of the measured pressure. Unlike the other devices described above, this sensor was operated remotely through a wired cable. Thus, continuous measurement was possible by using a cable long enough for the borehole depth.

The water pressure sensor was installed on 9th January into BH1 and on 18th January into BH3. Measured pressure data were transferred to the glacier surface through a 700-m-long wired cable and recorded with a datalogger CR1000 (Campbell Scientific, Inc.). The sensor and the data logger were operated with a 12 V rechargeable battery connected to a solar charger system. We enclosed the datalogger and the 12 V power supply into a water proof container, and placed it on the glacier surface near by the boreholes.

### 3.1.3 Flow velocity

Surface flow velocity was measured at 4 locations in the study area with a global positioning system (GPS) from 3rd to 29th January, 2012. For this measurement, we used two types of dual-frequency GPS receivers, System1200 (Leica Geosystems AG) and GEM-1 (GNSS Technologies Inc.). We used a static positioning technique of the carrier-phase differential GPS. This method was employed as high accuracy was required for short-term velocity variations and small displacement in the vertical direction. The GPS positioning error is dependent on the baseline length between reference and measurement stations. Commonly used estimate of the measurement error of this method is a function of the baseline length as  $(5 + 1 \text{ ppm}) \text{ mm}$  (Sada, 2003).

The GPS receivers for measurement stations were mounted at the top of 1.5-m long aluminum poles, which were drilled into the glacier surface at 0.4–3.3 km from the terminus (Fig. 2-1, GPS1–4). A steam drill was used to drill a hole to install the poles. To survey these poles, we used two types of the GPS receivers: GEM-1 and System1200. Each of the GPS receivers was enclosed in a waterproof box with a 12 V rechargeable battery connected to a solar panel. These boxes were placed on the glacier near-by the GPS antenna poles. As a reference station, another GEM-1 antenna, receiver and solar battery system were fixed on bedrock to the west of the glacier (Fig. 2-1, GPS FIX) to serve as a reference station. Installing this reference station nearby the glacier was crucial to improve the accuracy of the GPS positioning. The baseline lengths to the measurement stations were 3.1–3.6 km.

The two types of GPS receivers were operated in slightly different manners depending on their energy consumption rates. The Leica receivers were operated with a program, so that GPS satellite signals were recorded for 30 minutes every hour. The GNSS receivers were run continuously. The GPS data were stored in a flash memory card and post-processed with a static positioning technique to compute three-dimensional coordinates of the measurement station by Leica GeoOffice (Leica

Geosystems AG). Data from both receivers were processed to obtain hourly coordinates of the antennae and flow velocities were computed from displacements and the measurement interval. In general, this technique provides precise coordinates relative to the reference station with errors of 2–3 mm in horizontal and 5 mm in vertical directions. Accordingly, errors in the computed velocity were less than  $0.1 \text{ m a}^{-1}$ , which is negligible as compared to measured annual velocity.

#### 3.1.4 Surface elevation

Glacier surface elevation was measured in the field on 24th and 25th January, 2012. We used the same reference GPS station as for the flow velocity measurement. On the glacier, the Leica GPS receiver was operated as a rover station to use the kinematic positioning technique for this purpose. A reported positioning error of the kinematic positioning is a linear function of the base line ( $20 + 2 \text{ ppm}$ ) mm (Sada, 2003). For this measurement, we estimate a positioning error up to 30 mm, which is smaller than the surface roughness generally observed in the survey region.

The antenna of the Leica GPS (Leica Geosystems AG, System1200) was fixed at the top of a 2-m-long survey pole to serve as a rover station. The antenna was connected to a receiver in a backpack, and the GPS satellite signals were continuously recorded every second while a surveyor walk around on the glacier. We stopped at each measurement point and set the survey pole vertically on a glacier surface for 15 seconds. The positioning data were averaged for this time period. We surveyed 382 locations over the region, approximately every 100 m along 7 survey routes (Fig. 2-1). Additionally, surface elevations were also surveyed at the measurement sites of the flow velocity (GPS1–4). The GPS data were processed to obtain three-dimensional coordinates of the survey points by using Leica GeoOffice. In general, the kinematic positioning technique provides coordinates of antenna with positioning accuracies of 10 mm.

### 3.1.5 Ice thickness

Ice thickness of the terminus region was measured from 25th January to 5th February, 2012. We used an ice radar system manufactured by Department of Geography at Ohio State University. The radar system is composed of a transmitter, a receiver and 20-m-long antennae, which follows the design by Vickers and Bollen (1974). This system was previously used in many mountain glaciers in other regions (e.g. Fukuda and others, 2011). The transmitter generates and radiates 5-MHz of electromagnetic waves as a short pulse. The antenna of the receiver captures the direct wave (propagated through surface air) and reflected wave (penetrated through glacier ice). The ice thickness can be calculated by the delay time between the direct and reflected waves and a propagation speed in glacier ice. The received waves were digitized and stored by a digital oscilloscope: THS720 std (Tektronix, Inc.) and a laptop computer.

For this measurement on the glacier, we kept a distance of 20 m between the transmitter and receiver. We defined the midpoint between the transmitter and the receiver as the measurement site of ice thickness. The coordinates of the measurement sites were measured by the kinematic GPS technique at the same time as the ice radar measurement. The ice thickness measurement was carried out along a longitudinal profile which follows ice flow direction and 5 profiles to the transverse direction. These profiles were set within a region where relatively few crevasses were observed. The measurements were performed approximately every 100 m along the profiles (Fig. 2-1).

The propagation speed of the electromagnetic wave is  $300 \text{ m } \mu\text{s}^{-1}$  in the air, whereas it is not exactly known in glacier ice. The speed is determined by the permittivity of ice, and thus influenced by physical properties and mechanical structure of ice, such as temperature, impurities, crevasses and voids. Because of this reason, the propagation speed was calculated from a calibration measurement at one of the drilling sites, where ice thickness is known after the drilling. As we describe later, ice thickness

at Site 1 was 398 m according to borehole observations. At this location, a reflected wave was observed after 4.35  $\mu\text{s}$  of the direct wave. Relying on this information, the propagation speed within the Langhovde Glacier was assumed to be 181.4  $\text{m } \mu\text{s}^{-1}$ . The ice thickness was calculated by the following equation.

$$d = \sqrt{\left(\frac{vt}{2}\right)^2 - L^2}, \quad (\text{eq. 3-3})$$

where  $d$  (m) is the ice thickness,  $v$  is the propagation speed in the glacier ( $= 181.4 \text{ m } \mu\text{s}^{-1}$ ),  $t$  ( $\mu\text{s}$ ) is the measured delay time at each point, and  $L$  is the half of the distance between the transmitter and receiver ( $= 10 \text{ m}$ ). The uncertainty of this measurements is less than 10 m (Matsuoka and others, 1999).

### 3.1.6 Meteorological observation

Local weather on the glacier was observed from 2nd to 29th January, 2012. We used an automated weather station (AWS) CVS-WXT520 (Vaisala Inc.) for this measurement. This instrument is equipped with a wind direction and speed, air temperature, humidity and atmospheric pressure sensors within a single housing. The AWS was mounted at the top of a 3.0-m long aluminum pole. The pole was drilled into the glacier ice more than 1.5 m deep to prevent the AWS from moving and rotating during the measurement period. The height of the AWS device from the ice surface was 1.50 m. The 10-minutes averaged meteorological data were stored in a general-purpose datalogger CR1000 and downloaded to a computer connected by a RS-232C cable. To operate this device, a 12 V rechargeable battery connected to a solar panel and a battery charger was enclosed into a waterproof box with the datalogger.

## 3.2 Results

### 3.2.1 Hot-water drilling

At the two drilling sites, we drilled four boreholes in total during the field campaign. These boreholes were confirmed to reach the glacier bottom as described later. The boreholes were about 40 cm in diameter at the surface. The hole is narrower in the deeper region, because the wall of the hole melts during the drilling and this effect enlarges the hole in the upper region. Each of the borehole drilling operations took 8–10 hours, and the rate of the drilling was 34–40 m h<sup>-1</sup> (Fig. 3-2). The first borehole at Site 1 (BH1) was narrower than the other holes because we used the pulley and tripod system instead of the winch, which resulted in faster drilling than the other boreholes. Because of this reason, borehole measurements in this borehole were limited. Then, we employed the winch and drilled at slower rate at BH2 and BH3, resulting in smoothly-shaped boreholes with greater diameters. These boreholes allowed us to perform various measurements at least for several days. BH4 was drilled at a faster rate than those at BH2 or BH3, because we intended to install only a small-sized water pressure sensor.

### 3.2.2 Borehole observations

- Borehole camera

Borehole camera observations provided images of the boreholes, water cavity beneath the glacier, and the bottom of the cavity (Fig. 3-3). It was confirmed by the images that the borehole was drilled straight down with a uniform shape for 398–431 m from the surface. We found a 24–10 m thick water layer under the glacier ice. This subglacial water was found to be saline water after the CTD measurements described in the next subsection. Glacial sediment and clayey silt were covering the bottom of the water layer. The deposited silt stirred up by the motion of the borehole camera was flowing to the horizontal direction by water currents. According to a measurement of current, the saline water flows slowly in one direction at a rate of 2–3 cm s<sup>-1</sup> (Sugiyama and others, 2013). Additionally, the borehole cameras caught a benthonic organism (Fig. 3-3). The animal came into the frame of the camera probably because it was attracted by the LED light. This organism is a crustacean which is commonly observed around Antarctica, and a similar animal was observed beneath a larger ice shelf in West Antarctica (Lipps and others, 1979). However, this observation was the first time to find such animal close to the grounding line of the ice sheet. We also found other living animals and phytoplankton in the subshelf environment (Sugiyama and others, 2013).

- CTD profiler

Our CTD measurements provided information of water properties in the borehole and the subglacial environment. The water in the boreholes from water surface to the glacier bottom was fresh, whereas saline water fills the space between the glacier sole and the bottom of the water. The salinity in the water layer under the glacier was 34.25 PSU (Fig. 3-4). We found little salinity variation in the vertical direction in the water layer. Although salinity was nearly uniform throughout the water column from top to bottom, it slightly decreased near the glacier bed.

Water temperature of the fresh water in the boreholes was kept at the pressure melting point (Fig. 3-4). The water temperature was 0 °C at the water surface and decreased with the depth at a rate of  $-0.07$  °C per 100 m. We found a remarkable jump in the water temperature at the boundary between the fresh water and the saline water. The temperature of the fresh water in the borehole was  $-0.26$  °C near the bottom of the glacier, whereas the mean temperature of the subshelf saline water was  $-1.45$  °C.

The salinity and temperature of the subglacial water (34.25 PSU and  $-1.45$  °C) were similar to those previously measured in the nearby ocean. According to Ohshima and Kawamura (1994) which reported results of CTD measurements in front of the glacier several kilometers from the calving front, the salinity and temperature at 400.01 dBar pressure (same depth as the glacier bed) was 34.21 PSU and  $-1.53$  °C, respectively. The differences between these values from our measurements are within seasonal variability expected in this region (Ohshima and others, 1996). Similar values were also reported by Ushio and Takizawa (1993). These facts suggest an active transport of sea water from open ocean into the subshelf cavity.

- Water Pressure

The variations in the subglacial water pressure measured in the borehole are shown in Fig. 3-5. We found that the water pressure periodically-varied with time. The variation range was  $1.64 \times 10^{-2}$  MPa, which corresponds to 1.68 m of fresh water level change. The timing and the magnitude of the water pressure changes corresponded exactly to the tides measured in front of the glacier. The ocean tide measurement was performed at about 4 km from the calving front by one of the JARE 53 member, Noriaki Izumi (personal communication). The agreement between the subglacial water pressure and the tide confirms that the subglacial cavity was hydraulically connected to the open ocean.

### 3.2.3 Flow velocity

The surface flow velocity is shown in Table 3-1 and Fig. 3-6. The fastest velocity was  $130 \text{ m a}^{-1}$  at GPS1 near the terminus. At GPS4, which is the uppermost measurement site, ice flows at a rate of approximately  $100 \text{ m a}^{-1}$ . The flow velocity decreased gradually with the distance from the terminus, which is a typical ice flow regime on a floating tongue of an outlet glacier.

The horizontal flow velocity and vertical displacement at each of the GPS sites are shown in Fig. 3-7. In GPS1–2, flow velocity and vertical displacement increased twice a day. These variations are correlated with the water level in the borehole. Thus, the ice flow and vertical motion were controlled by tides.

#### 3.2.4 Surface elevation

Surface elevation along the survey profiles in the 5 transverse and longitudinal directions were depicted in Fig. 3-8. The survey results revealed a nearly flat terrain along IR1. Difference between the highest and lowest elevation along the 1.5 km survey route along the flow line is only 7 m. The flat surface suggests that the terminus region forms a floating tongue. The longitudinal profile shows that the elevation increases with the distance from the terminus. The mean slope over the 1.5 km long survey route was  $0.27^\circ$ . In contrast to the flat surface near the terminus, elevation increases by 25 m along the flow line from 1.5 to 3.0 km from the terminus, which is equivalent to the slope of  $0.95^\circ$ .

### 3.2.5 Ice thickness

Fig.3-9 shows ice radar waveforms obtained along the most downstream and upstream profiles (IR1 and IR5). The signals of reflected waves can be identified clearly in the eastern side of IR5. The delay time varies from point to point, showing ice thickness variations. As compared to the eastern side, the signals from the bedrock in the western side of IR5 were less clear. This was because the glacier ice was relatively thicker in this region. The reflection signals were difficult to identify at most of the measurement sites along IR1. This was probably because of a crevasse zone near the glacier front, which disturbs the measurements by reflections at ice-air interfaces within the glacier. Ice thickness was computed only for the waveforms in which bedrock reflections were clearly identified. The obtained thicknesses data were shown in Table 3-2 and Fig.3-10. The results indicate that ice thickness was from  $170\pm 10$ m near the terminus and up to  $450\pm 10$  m in the central part of the uppermost profile.

### 3.2.6 Meteorological observation

The meteorological data obtained on the glacier surface were shown in Fig. 3-11. Air temperature frequently exceeded 0 °C during the day time on fine days. The maximum daytime temperatures exceeded 0 °C in 28 times during 6th January to 7th February, 2012. Mean temperature was -1.6°C and the range of the temperature variations during the measurement period was from -11 °C to 8 °C. Snow stake measurements show a relatively-large amount of ablation due to the warm temperatures (Table 3-3). These observations agree with our observations that meltwater running on the surface along supraglacial channels. Wind speed was generally less than 5 m s<sup>-1</sup>, except for the storm weather (> 20 m s<sup>-1</sup>) on 14th, 23rd, 26th–27th, and katabatic wind (~15 m s<sup>-1</sup>) in the late afternoon. The katabatic wind blowing down the inclined ice sheet surface was across the glacier from east to west.

### 3.3 Estimation of the bed elevation

The vertical cross section of the Langhovde Glacier revealed by our field measurements is illustrated in Fig. 3-12. This figure is based on the results obtained by the ice radar, GPS survey and borehole measurements. In Fig. 3-12, the elevation of the glacier sole which was estimated from the assumption of hydrostatic equilibrium was plotted by dashed-dotted line. The hydrostatic equilibrium condition is the balance of the gravitational and buoyancy forces acting on a floating ice. Under the hydrostatic equilibrium, the depth of the glacier bed was calculated using the following equation.

$$d = \frac{\rho_i}{\rho_w - \rho_i} h \quad , \quad (\text{eq. 3-4})$$

where  $d$  is the depth of the glacier bed,  $\rho_i$  and  $\rho_w$  is the densities of the glacier ice and sea water and  $h$  is the surface elevation relative to the water surface. Usually, the density of the glacier ice has to be determined by the thickness and the density of firn covering the surface. However, in the studied region, most part of the glacier surface is bare ice because ice melts during summer time and winter snow precipitation is blown away by strong katabatic wind. Occasional snow cover layer is very thin. For this reason, we assume that the density of the glacier in the terminus region is the same as pure ice density ( $917 \text{ kg m}^{-3}$ ) (Gow, 1970). The density of sea water was calculated by an equation proposed to describe the state of seawater (UNESCO, 1981). The equation required the salinity, temperature and pressure of sea water which were known in our case by the subglacial CTD measurements. According to the salinity (34.25 PSU), temperature ( $-1.5 \text{ }^\circ\text{C}$ ) and pressure (398 m w.e. = 39.03 bar), the density of sea water was calculated as  $1029 \text{ kg m}^{-3}$ .

The estimated glacier bed under the hydrostatic equilibrium was compared with the measured bed (surface elevation – ice thickness) obtained by the ice radar survey. The estimated glacier bed is agreed with the measured glacier bed within an error of  $\pm 10$  m in the most part of the terminus region. In this region, tidally induced vertical ice motion was observed at two of the GPS stations (GPS1–2) (Fig 3-7). These observations strongly suggest that the terminus was in a floating condition, and the hydrostatic equilibrium was established. However, there is difference between the estimated and measured bed elevations at GPS3–4. Hydrostatic equilibrium condition is not met at these locations nearby the drilling sites. At GPS3, the glacier surface was below a level expected under the floating condition, suggesting that there is downward force acting in vertical direction from nearby ice mass. In contrast to this situation at GPS3, the surface at GPS 4 was above the level expected for floating ice. This suggests a possible pitfall in the determination of the grounding line from surface observations. The surface elevation above sea level and ice thickness indicate the ice is grounded at GPS4, but our borehole observations confirm the existence of the subglacial water layer.

Based on these observational results, we propose that the grounding line of the Langhovde Glacier has more complex structures as it has been assumed in previous studies. Subglacial water layer penetrates further upstream than it is estimated from the surface observations, which means the glacier sole is in contact with ocean water over a greater area. Thus, our findings suggest the importance of interaction with subglacial ocean water in the evolution of the Langhovde Glacier. More detailed discussion on the grounding position is given later in chapter 5.1.

Table 3-1 Results of flow velocity measurement.

Point	Latitude	Longitude	Velocity ( $\text{m a}^{-1}$ )		Period
			(horizontal)	(vertical)	
GPS1	69°11'03.46"S	39°47'01.61"E	129.26	-1.95	7-29 Jan., 2012
GPS2	69°11'37.06"S	39°47'51.44"E	112.21	0.40	5-29 Jan., 2012
GPS3	69°12'10.33"S	39°49'22.87"E	110.51	-3.06	3-29 Jan., 2012
GPS4	69°12'23.28"S	39°49'33.84"E	101.80	-3.33	12-29 Jan., 2012

Table 3-2 Coordinates and ice thickness data at survey points of the radar sounding. The ice thickness marked by \* indicated a reference thickness for calculating propagation speed.

Profile	Latitude	Longitude	Elevation (m)	Ice thickness (m)
IR1	69°11'12.64"S	39°47'46.28"E	27.8	260
	69°11'14.07"S	39°47'39.00"E	28.9	284
	69°11'15.70"S	39°47'31.24"E	28.7	282
	69°11'17.21"S	39°47'23.31"E	28.3	225
IR2	69°11'30.70"S	39°48'48.26"E	33.0	301
	69°11'31.50"S	39°48'39.91"E	30.4	280
	69°11'32.27"S	39°48'32.05"E	33.6	273
	69°11'33.47"S	39°48'24.51"E	36.2	277
	69°11'34.45"S	39°48'16.38"E	32.1	286
	69°11'35.07"S	39°48'08.43"E	30.9	313
	69°11'36.11"S	39°47'59.58"E	27.9	289
	69°11'37.10"S	39°47'51.53"E	31.9	273
69°11'38.33"S	39°47'43.22"E	32.4	265	
IR3	69°11'44.30"S	39°49'28.10"E	27.7	290
	69°11'50.03"S	39°49'07.74"E	34.4	278
	69°11'51.40"S	39°48'59.95"E	36.9	290
	69°11'53.37"S	39°48'51.31"E	38.7	296
	69°11'57.12"S	39°48'37.85"E	44.3	317
	69°11'58.64"S	39°48'30.59"E	47.6	311
	69°12'08.97"S	39°47'51.40"E	54.4	411
	69°12'09.07"S	39°47'43.19"E	50.8	403

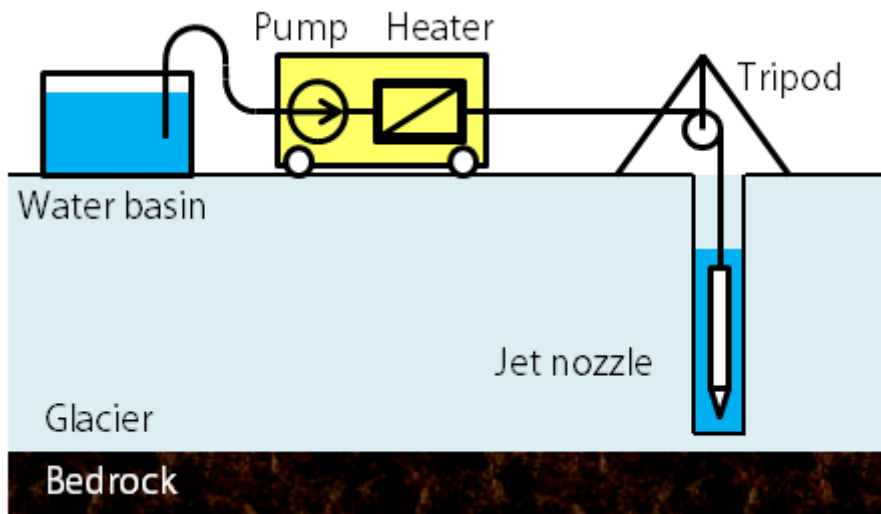
(Continued on the following page.)

Profile	Latitude	Longitude	Elevation (m)	Ice thickness (m)
IR3	69°12'09.88"S	39°47'34.42"E	45.4	357
	69°12'10.85"S	39°47'25.81"E	39.4	335
	69°12'12.03"S	39°47'15.69"E	34.1	328
	69°12'16.75"S	39°46'49.09"E	33.0	318
	69°12'17.69"S	39°46'139.87"E	33.4	295
IR4	69°11'57.64"S	39°49'58.72"E	36.8	309
	69°12'05.85"S	39°49'36.08"E	42.1	311
	69°12'08.05"S	39°49'29.74"E	42.7	330
	69°12'10.28"S	39°49'22.67"E	42.8	398 (*)
	69°12'12.26"S	39°49'16.20"E	48.3	372
	69°12'14.24"S	39°49'09.91"E	51.2	374
	69°12'25.23"S	39°48'23.04"E	48.4	359
	69°12'26.65"S	39°48'15.06"E	43.5	339
	69°12'28.02"S	39°48'06.55"E	39.4	329
	69°12'29.32"S	39°47'58.98"E	37.1	333
	69°12'30.83"S	39°47'50.94"E	35.8	315
	69°12'32.18"S	39°47'44.06"E	35.9	306
	69°12'33.67"S	39°47'35.55"E	37.6	295
	69°12'35.01"S	39°47'27.42"E	39.1	263
69°12'36.58"S	39°47'19.79"E	33.2	258	
IR5	69°12'05.85"S	39°48'56.54"E	53.5	446
	69°12'08.05"S	39°48'48.53"E	51.0	440
	69°12'10.28"S	39°48'40.72"E	49.4	386
	69°12'12.26"S	39°48'33.17"E	45.5	353
	69°12'14.24"S	39°48'25.47"E	44.1	338
	69°12'25.23"S	39°48'17.17"E	44.2	342
	69°12'26.65"S	39°48'08.48"E	43.4	317
	69°12'28.02"S	39°48'00.91"E	43.9	300
	69°12'29.32"S	39°47'52.75"E	47.9	288
	69°12'30.83"S	39°47'43.59"E	44.1	260
69°12'32.18"S	39°47'34.91"E	43.2	242	

Table 3-3 Melt rate at GPS measurement points.

	Period	Melt (m)	Melt rate (m a <sup>-1</sup> )
GPS1	7–29 Jan., 2012	0.070	1.18
GPS2	7–29 Jan., 2012	0.090	1.52
GPS3	–	–	–
GPS4	12–19 Jan., 2012	0.025	1.39

(a)



(b)

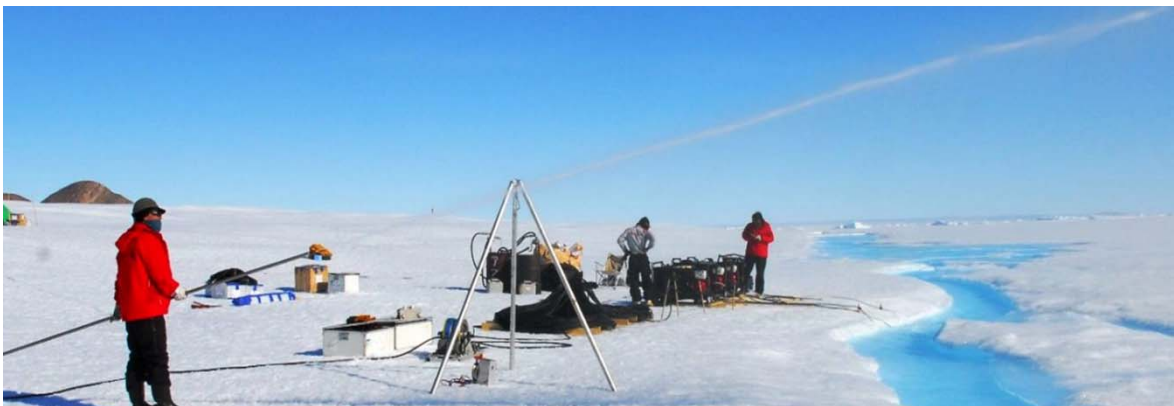


Fig. 3-1 (a) Schematic diagram of a hot water drilling system. The hot water drilling system consists of high-pressure water pump, heater, hose and jet nozzle which were supported by winch, tripod and pulley. Water basin was used as water source when supraglacial stream is not available. (b) Photograph showing hot-water drilling at Site 1 on the Langhovde Glacier. Melt water was pumped up and heated to a high temperature by the high pressure hot water machine in the middle right of the photograph.. The hot-water jet was ejected from the tip of nozzle.

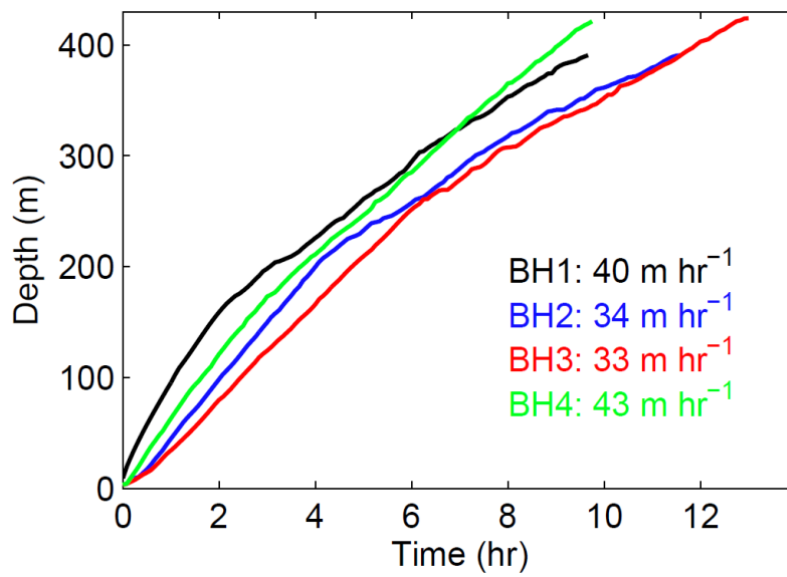


Fig. 3-2 Drilling speed of hot-water drilling at the Langhovde Glacier. BH1 and BH2 were drilled at Site 1, and BH3 and BH4 were drilled at Site 2.

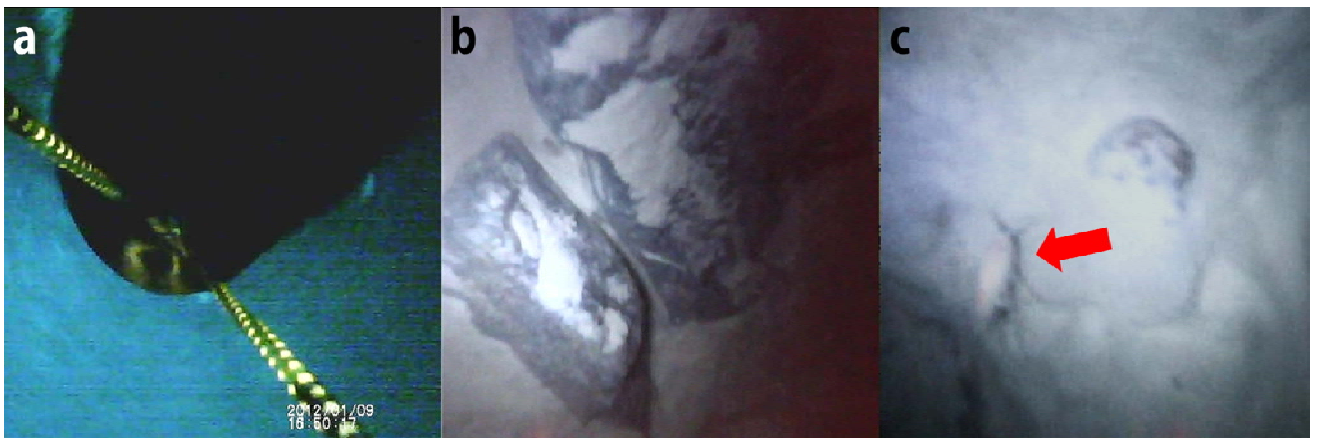


Fig. 3-3 Images obtained by the borehole camera observations at BH2. (a) The lowest part of borehole at 398 meters below surface. (b) The bottom of the subglacial water layer (422 meters below surface). (c) The cameras caught a benthonic organism.

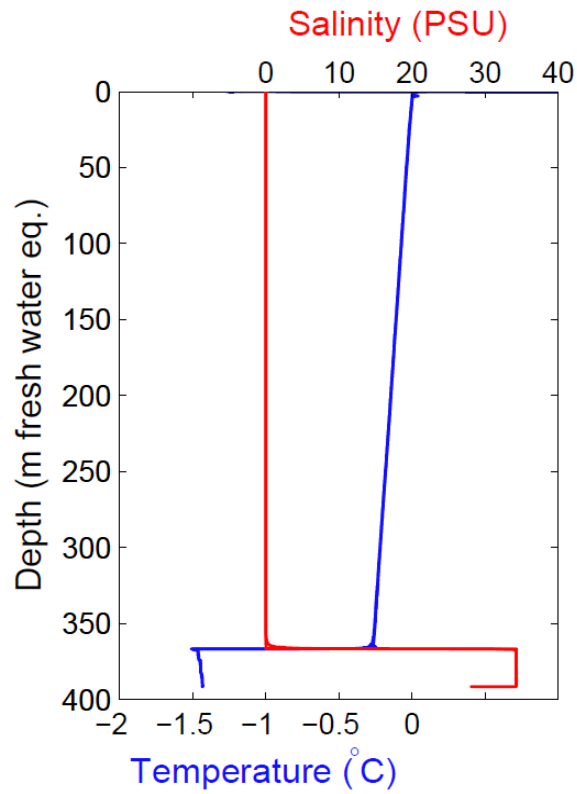


Fig. 3-4 Vertical profiles of salinity (red) and water temperature (blue) measured in BH2.

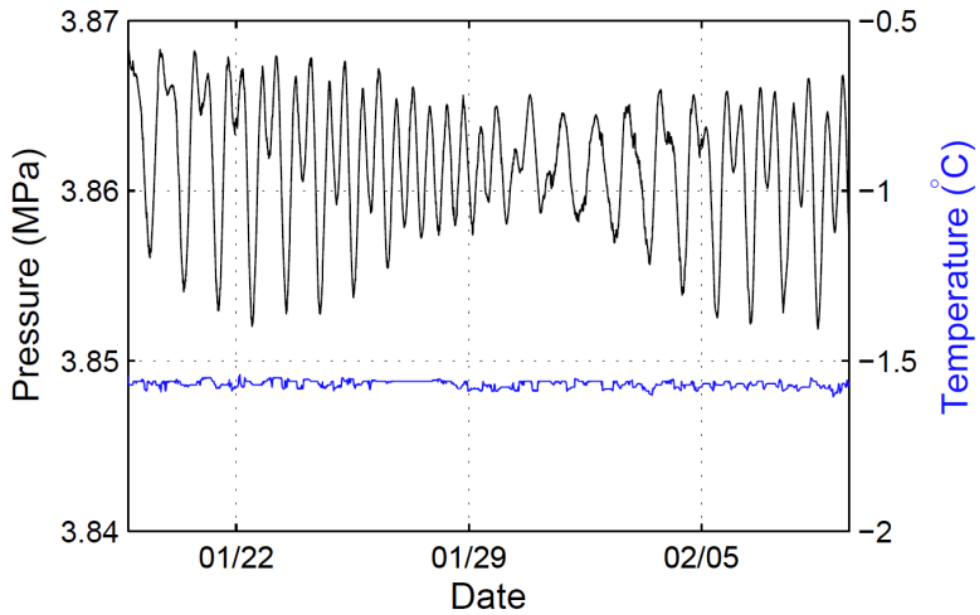


Fig. 3-5 Variations of water pressure (black) and temperature (blue) measured in the subglacial water layer in BH1.

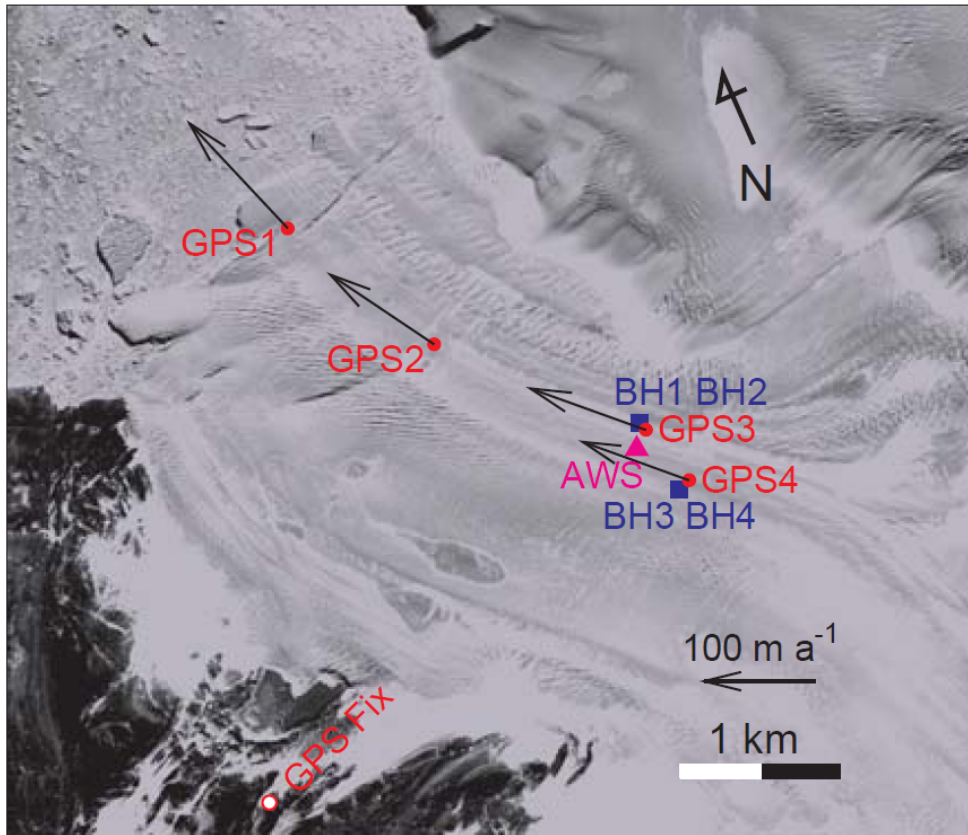


Fig. 3-6 Horizontal flow velocity vectors measured by the GPS survey. Locations of the GPS measurement stations and the reference station are indicated by filled red circle and open red circle, respectively. Borehole drilling sites are shown by the blue squares.

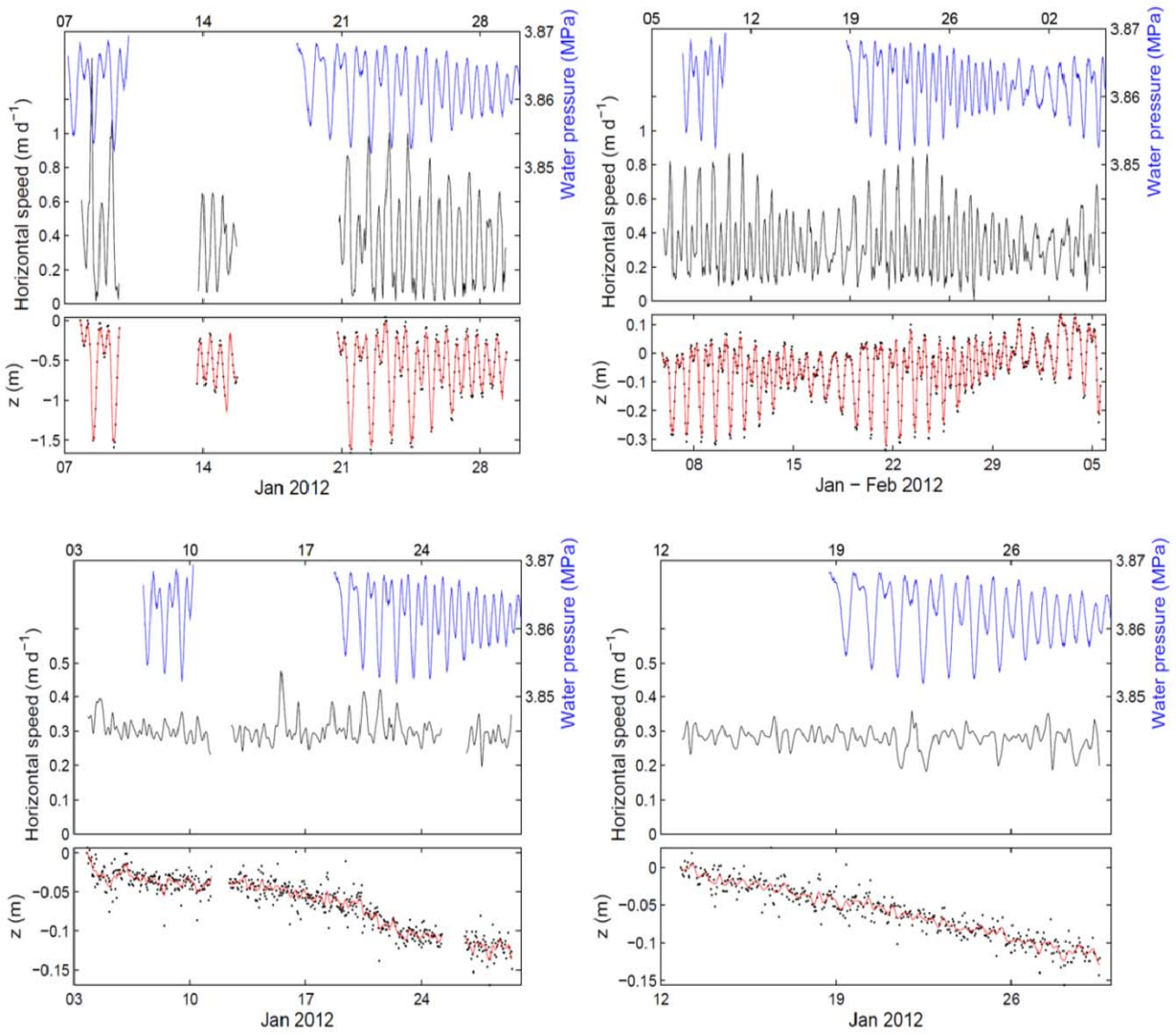


Fig. 3-7 Horizontal ice speed (black) and vertical motion (red) at (a) BH1, (b) BH2, (c) BH3 and (d) BH4. Subglacial water pressure measured in BH1 is plotted in blue.

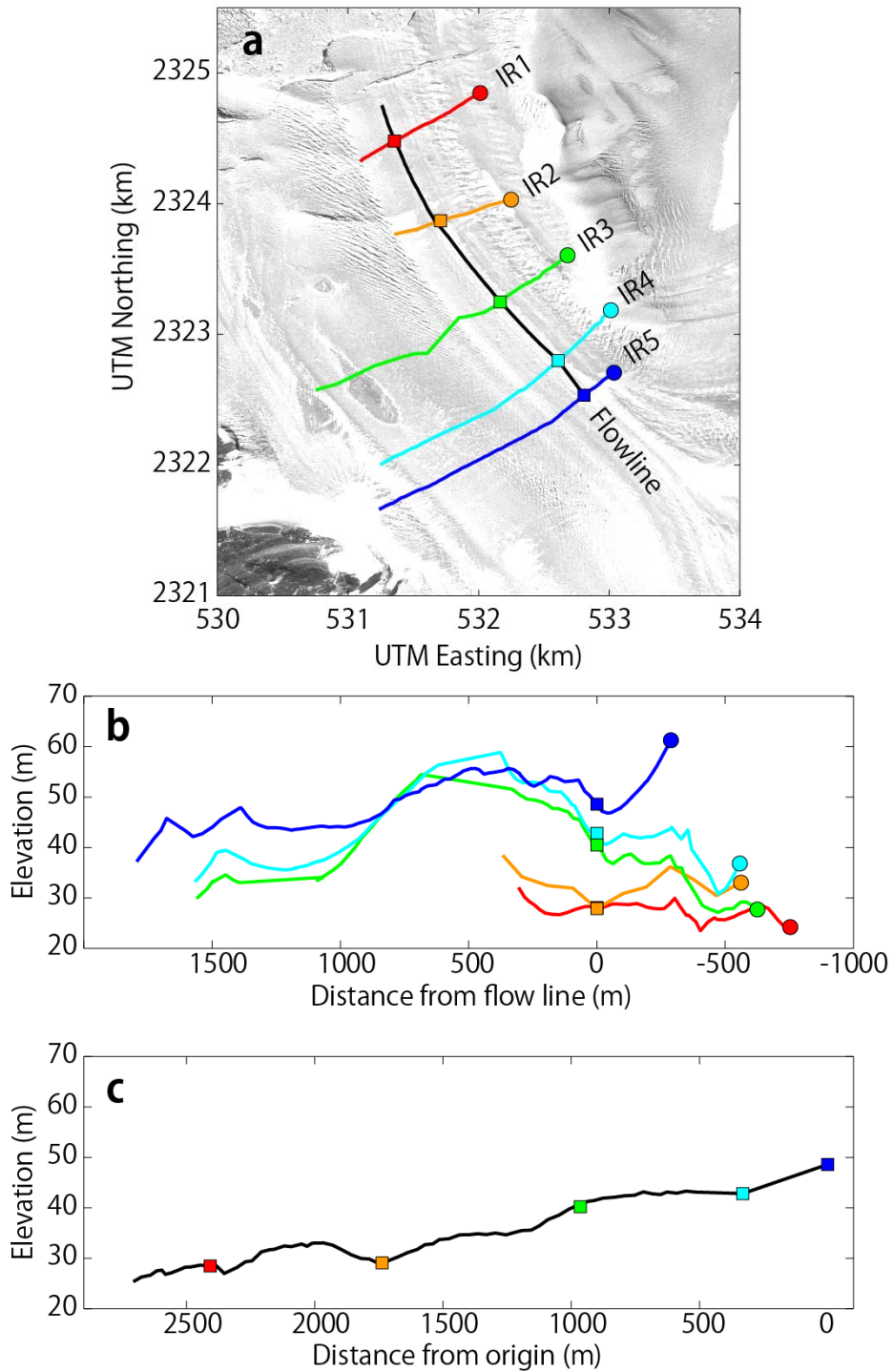


Fig. 3-8 Surface elevation measured along the survey routes. (a) Location of survey route. (b) Traverse profile (red: IR1, orange: IR2, green: IR3, cyan: IR4, blue: IR5). (c) Longitudinal profile along the flow line (black). Markers on the profile indicate origin of profile (circle) and intersection point of profile, respectively.

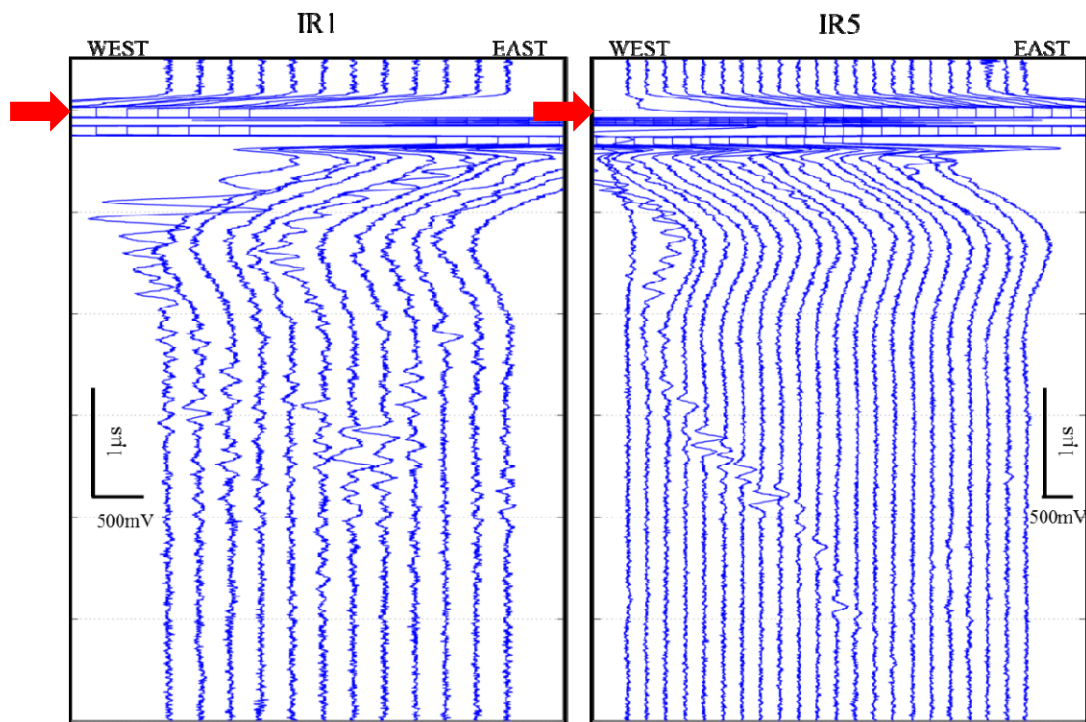


Fig. 3-9 Stacked waveforms of the ice radar measurement along IR1 (left) and IR5 (right). The waveform has major two peaks which represent the direct wave (red arrow) and reflection from the bed after only a few micro seconds of the direct wave.

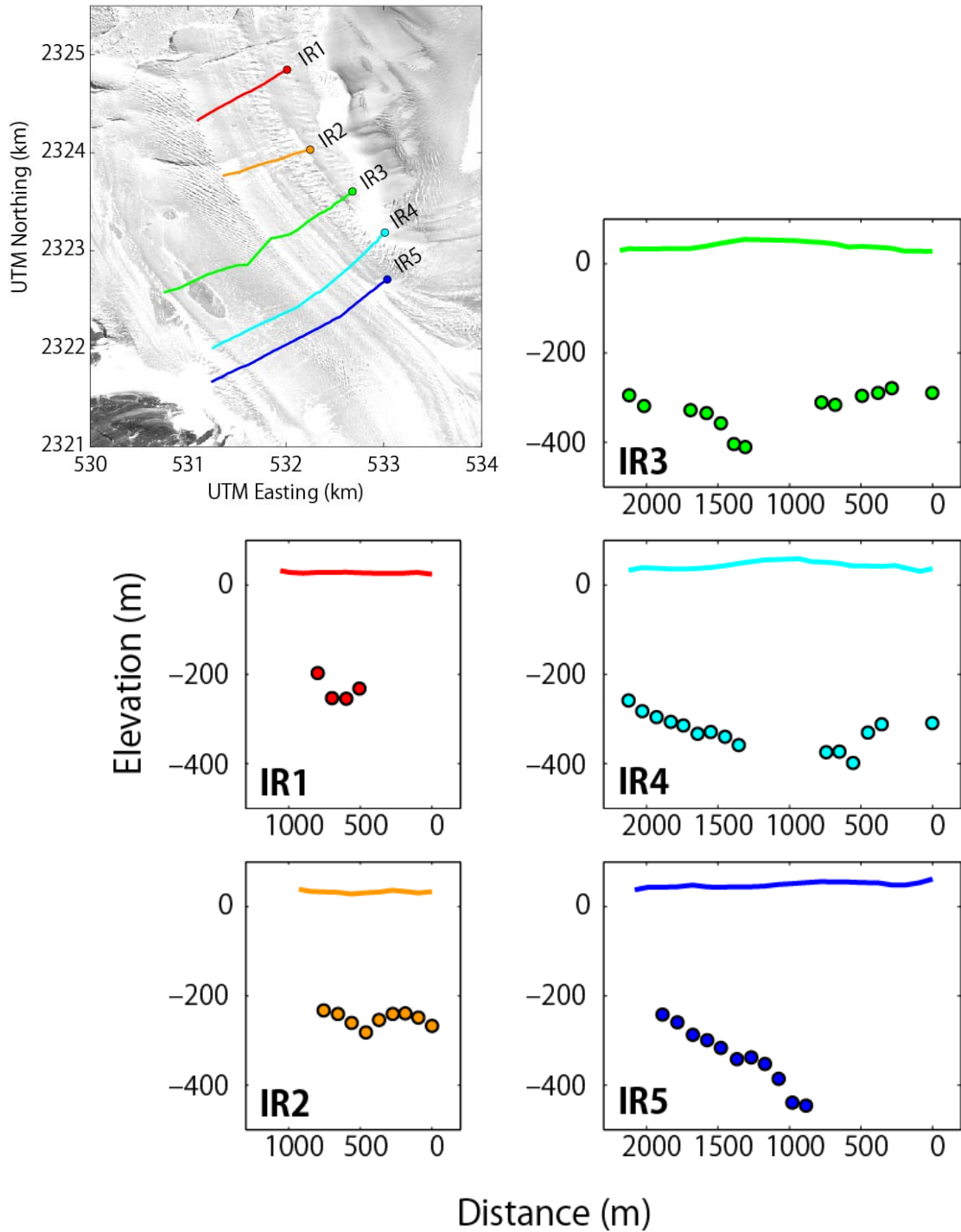


Fig. 3-10 Vertical cross-section in traverse direction. Solid line and circles denote the surface elevation and measured ice thickness by radar sounding, respectively.

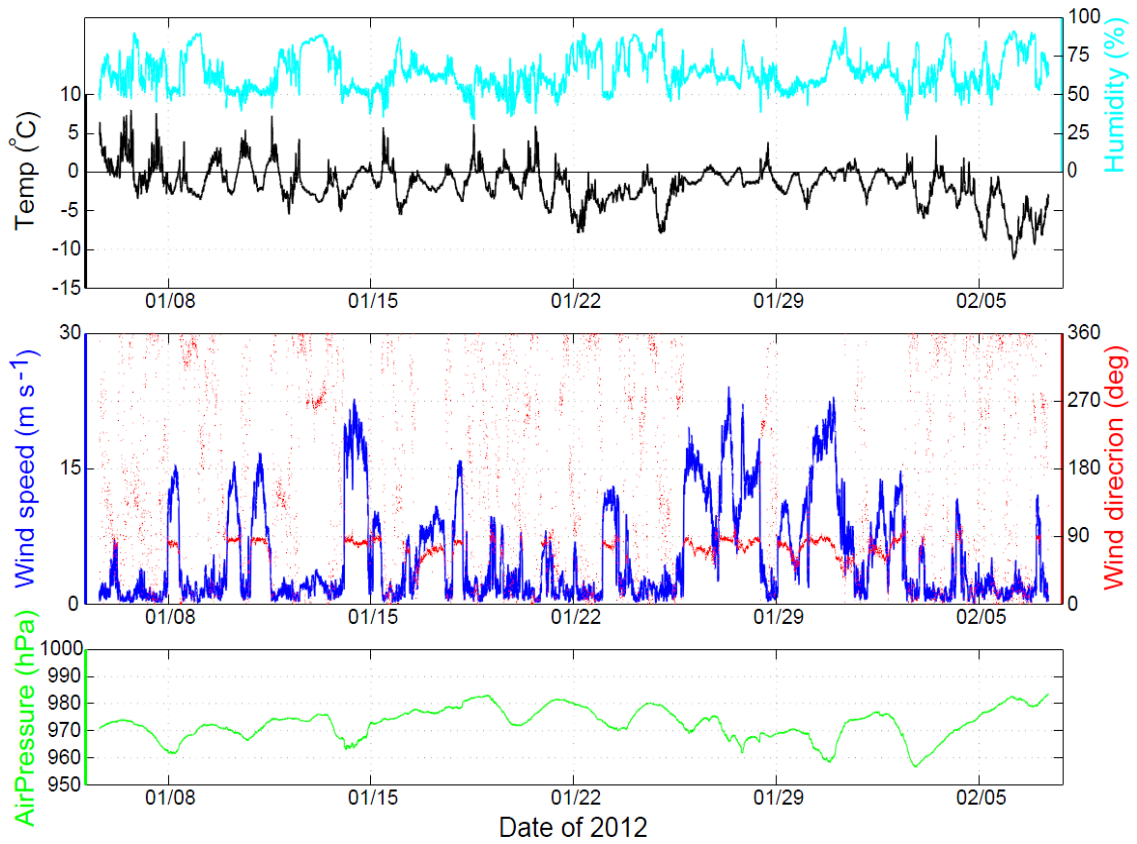


Fig. 3-11 (a) Air temperature (black) and relative humidity (cyan), (b) wind speed (blue) and wind direction (red) and (c) air pressure (green), measured by the AWS installed on the Langhovde Glacier.

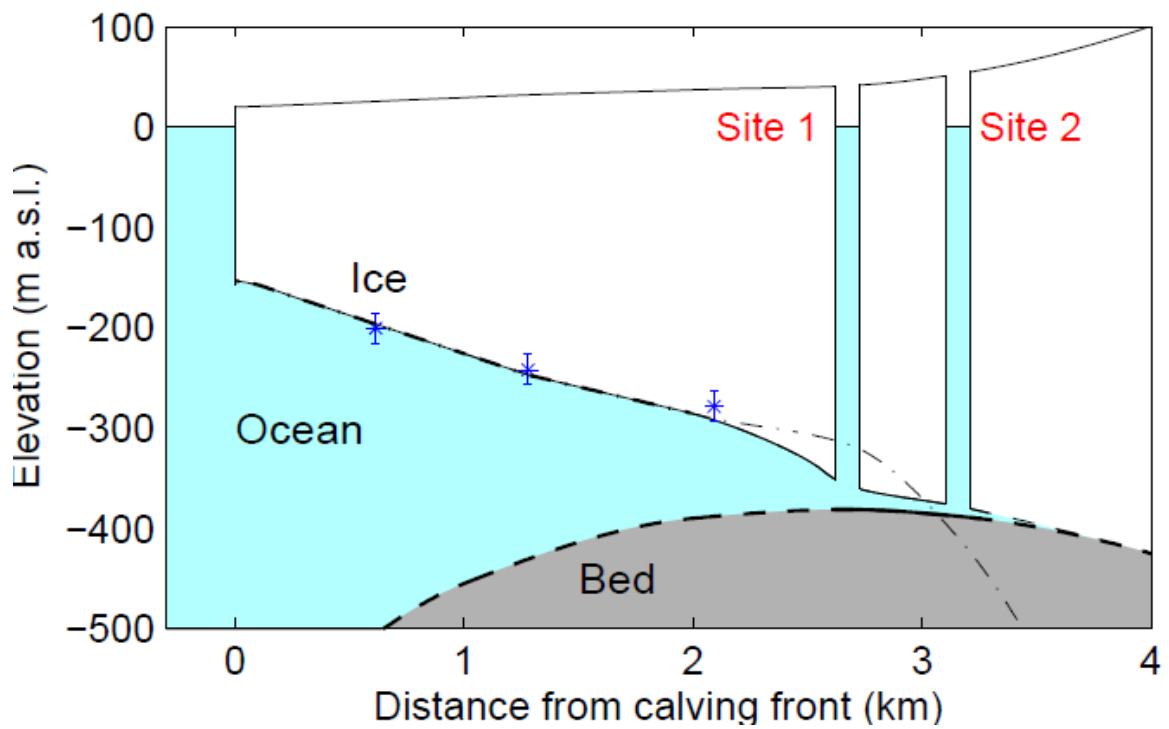


Fig. 3-12 Cross-section of the glacier in the longitudinal direction. Dashed-dotted line shows the glacier bed profile under the assumption of the hydrostatic equilibrium. The depths of ice bottom measured by the ice radar measurement were indicated by asterisks.



## ***Chapter 4     Satellite image analysis***

### **4.1    Methods**

#### **4.1.1    Terminus position**

Changes in the terminus position of the Langhovde Glacier were analyzed with a series of satellite images covering a period between 2000 and 2012 (Fig. 4-1). We used panchromatic band 8 images obtained by the Enhanced Thematic Mapper Plus (ETM+) mounted on Landsat7, and visible and near-infrared (VNIR) band 3N images obtained by the Advanced Spaceborne Thermal Emission and Reflection radiometer (ASTER) mounted on Terra.

These images are unavailable in polar regions during winter seasons, and thus data exist only for dates between 19th September to 6th April in the following year. The ETM+ images can be downloaded for free from Earth Explorer (<http://earthexplorer.usgs.gov>) provided by the U. S. Geological Survey. The ASTER-VNIR images were offered by AIST (Advanced Industrial Science and Technology) under collaboration with Dr. Kazuki Nakamura (Nihon University). These images were available on ASTER GDS - DAR (The ASTER ground data system - data acquisition request) system (<http://ims.aster.ersdac.jspacesystems.or.jp/ims/html/MainMenu/MainMenu.html>) provided by Earth Remote Sensing Data Analysis Center. Specific dates and other information of the satellite images used for this purpose are summarized in Table 4-1. The spatial resolution of the both images is 15 m.

To obtain the mean displacement of the glacier calving front, we measured changes of the terminus area according to a technique proposed by Moon and Joughin (2008). An open-ended reference box which delineated with glacier width along the flow direction of the glacier was set on each image using GIS software (ArcGIS10, Environmental Systems Research Institute (ESRI), Inc.). And the glacier frontal margin was manually traced with the GIS software by clicking a computer mouse on a screen. By comparing the time series of satellite images within the delineated region, changes in the glacier surface area near the calving front (Fig. 4-2) were measured for time intervals. The mean displacement of the glacier front was determined by dividing the areal change of the reference box by the width of the calving front. Potential errors in the measurement include misalignment of the satellite images and uncertainties in the manual delineation process. We used 5 ground control points (GCPs) for each image pair to minimize misalignment. The GCPs listed in Table 4-1 were obtained from 1:25,000 Topographic Maps for JARE (Geographical Survey Institute, <http://geogisopen.nipr.ac.jp/gisopen/>). The root mean square differences of GCPs were 23 m. Uncertainties in the delineation process were evaluated by repeating the procedure for one of the images, and the location of the calving front was compared. The standard deviation of the twenty measurements was 2.4 m. Thus, we assume the total error in this analysis is 25 m.

#### 4.1.2 Flow velocity

Flow velocities from 2003 to 2012 were measured by using a feature tracking analysis of the ASTER/VNIR images (Tobita and others, 2001). This method measures the rate of ice surface displacement, by tracking surface features (e.g. crevasses, ponds, channels), which are recognized on satellite images. We used the same type of the images as used for the terminus position measurements listed in Table 4-2. These images were trimmed 6×6 km square in the terminus area to improve the speed of processing. Displacements of ice surface features were measured using COSI-Corr, software provided by California Institute of Technology. This software is a plug-in for a remote-sensing platform ENVI (ESRI, Inc.), a geospatial imagery analysis and processing application. COSI-Corr calculates horizontal displacements of surface features by computing spatial correlations between a multi-temporal image pair with sub-pixel resolution (Leprince and others, 2007, Scherler and others, 2008, Harman and others, 2011). We chose 40 image pairs with intervals of approximately one year between 2003 and 2012. After the co-registration of an image pair, cross-correlation coefficients between the two images were computed within a reference window defined on the first image over a search window defined on the second image. The size of the reference window was 32×32–16×16, depending on the magnitude of the displacement.

As a result of this procedure, horizontal components of the surface displacement and the signal-to-noise ratio (SNR) were obtained over an area of 6×6 km near the glacier terminus with a spatial resolution of 15 m. The ASTER/VNIR images were orthorectified based on the DEMs supplied with the images, and the DEMs have relatively greater errors over a snow surface, low-contrast area and steep slopes. These errors in the DEM result in miscorrelations in the cross-correlation analysis. To minimize errors due to the miscorrelations, data with a SNR greater than 0.90 were removed and a median filter was applied to the displacement field. To compare the results with field data, flow velocities at the GPS measurement sites were computed by

interpolating the two-dimensional velocity fields.

The accuracy of the velocity measurements were evaluated by computing the displacement between images separated by a short period, a so-called null test (Berthier and others, 2012). Because displacement can be assumed to be negligibly small over a sufficiently short period, this analysis provides uncertainties in the measured displacement. By processing two image pairs with an interval of 2 days (10th–12nd October, 2008 and 14th–16th November, 2009), the standard error which arises from the cross-correlation analysis was determined to be 4.0 m. The separation of image pairs used for the velocity measurements were 0.65–1.32 year, thus, the uncertainty in the velocity was 3.0–6.2 m a<sup>-1</sup>.

#### 4.1.3 Surface elevation

Glacier surface elevation was measured by stereoscopic analysis of satellite images captured by the Panchromatic Remote-sensing Instrument for Stereo Mapping (PRISM) on the Advanced Land Observing Satellite (ALOS). The images used for this study were taken on 16th November, 2006, 29th November, 2007 and 10th November, 2010 (Table 4-3). The ALOS/PRISM images were radiometrically and geometrically corrected (Level 1B2) and accompanied with a rational polynomial coefficient file, which describes the parameters needed for converting the image pixels to geographical coordinates. The horizontal resolution of the image was 2.5 m.

The stereographic analysis was performed with a digital photogrammetry system, consisting of a stereo mirror 3D monitor (SD2020, Planar Systems, Inc.), 3D mouse (TopoMouse, Leica Geosystems AG) and Leica Photogrammetric Suite 2011 (LPS, Intergraph Corporation) mounted on an ERDAS IMAGE 2011 (Intergraph Corporation) platform. A stereo image pair was co-registered using one or more GCPs obtained from a 1:25,000 Topographic Map for JARE. The LPS automatically measure surface elevations from a stereo image pair to generate a polygonal surface, but this surface elevation data have substantial errors, particularly in low contrast regions such as snow surfaces, shadows and steep slope regions (Toutin, 2002). To improve accuracy, we manually corrected the elevation on the stereoscopic view using the 3D monitor and the 3D mouse. We also increased data points to improve spatial resolution, particularly for the regions with complex topography (Fig. 4-3). After this manual correction, a 10-m mesh DEM was generated by interpolating the polygonal surface (Lamsal and others, 2011). Spatial horizontal resolutions before the interpolation (the polygonal surface elevation model) were approximately 20 m.

To estimate the vertical errors in the generated DEMs, surface elevations of the DEMs were compared to a 1 km<sup>2</sup> snow free bedrock area. Because surface elevation does not change over this region, deviations of the data within each DEMs obtained

over the study period represent the ambiguity in the measured elevation. The mean standard deviation over the area was 3.2 m, similar to that reported in a previous study by Lamsal and others (2011).

## 4.2 Results

### 4.2.1 Terminus position

The glacier terminus advanced by 180 m from 2000 to 2012 after fluctuations within a distance of 450 m (Fig. 4-2). In the beginning of this time period, the glacier showed a sudden retreat of 170 m from 2000 to 2001 and 180 m in 2003. These events coincided with large calving events which occurred in the summer of 2000 and the summer of 2003. After these two events, the terminus advanced by 380 m from January 2007 to January 2010. During this period, large icebergs were not observed in front of the glacier. Another calving event occurred in January 2011, resulting in a 200 m retreat. The large calving events in 2000, 2003 and 2011 were captured by ASTER/VNIR images (Fig. 4-3). These images show the icebergs discharged by the events were approximately 750×250 m in size. The mean rate of glacier advance in the period from 2000 to 2012 was 15 m a<sup>-1</sup>.

#### 4.2.2 Flow velocity

Ice flow velocity map clearly shows fast flowing features of the Langhovde Glacier. A two-dimensional flow velocity field obtained for the period between 5th January, 2011 and 25th January, 2012 is shown in Fig. 4-5. The maximum velocity is  $128 \text{ m a}^{-1}$  observed at the glacier center near the terminus. The velocity field shows a main stream flowing into the region of interest from the south, and the velocity along the central flow line is greater than  $100 \text{ m a}^{-1}$ . The two tributaries merge with the main stream from the western flank of the glacier.

Velocity was interpolated at the GPS measurement sites to investigate temporal variations from 2003 to 2012 (Fig. 4-6). Our data show complex velocity variations over the study period, which are significantly greater than the measurement errors. At GPS2, velocity decreased from 2003/2004 to 2008/2009 by  $9.0 \text{ m a}^{-1}$ , followed by an increase of  $9.9 \text{ m a}^{-1}$  in the period from 2008/2009 to 2010/2011. The velocity dropped in 2011/2012, but the velocity obtained by the field GPS measurement in January 2012 was greater than the longer term mean velocity from October 2010 to February 2012. It should be noted that the field measurement represents the summer velocity, whereas the other satellite derived data are mean velocity over approximately one year. These changes are also observed at two other GPS sites. While the timings of the velocity changes are similar at the three locations, the acceleration from 2008 to 2009 initiated sooner near the terminus (GPS1) than the upper reaches (GPS2–4).

### 4.2.3 Surface elevation

Fig. 4-7 shows a shaded oblique view of a three-dimensional map of the Langhovde Glacier obtained by the ALOS/PRISM DEM in 2007. Changes in surface elevation were calculated by differentiation of two of such DEMs. Glacier surface elevation showed little variations over the study period. The rate of surface elevation change in the study region was from  $+4.9 \text{ m a}^{-1}$  to  $-8.8 \text{ m a}^{-1}$  between 2006 and 2010 (Fig. 4-8). There are several regions, where elevation change is greater than the vertical error of the DEMs (3.2 m). However, these changes are due to the advection of surface topographic features (e.g. crevasses, bumps and depressions) or snow deposition on a relatively steep surface. These surface features were observable on the satellite images, and also confirmed by in-situ observations during the field campaign 2011/2012. There is no general trend in the elevation change at the three GPS sites, as well as along the kinematic GPS survey routes (Fig. 4-9). The mean elevation change over the 382 survey locations along the survey routes was only  $-0.3 \text{ m a}^{-1}$  between 2006 and 2012. The magnitudes of the elevation changes were smaller than the DEM error. Thus, our DEM analyses and GPS field survey show no significant elevation change in the survey area from 2006 to 2012.

Table 4-1 Landsat7/ETM+ and Terra/ASTER images used to measure terminus position.

Period	Acquisition date ETM+ (6 images)	ASTER (57 images)
1999/00	15 Jan. 2000	
2000/01	9 Feb. 2001	16 Dec. 2000
2001/02		4 Jan. 2002
2002/03	6 Dec., 22 Dec. 2002	4 Nov. 2002, 8 Feb., 26 Feb., 14 Mar. 2003
2003/04		5 Nov., 2 Dec. 2003
2004/05		29 Sep., 27 Nov. 2004, 14 Jan., 26 Jan., 13 Feb., 24 Mar. 2005
2005/06		14 Nov., 12 Dec. 2005, 22 Jan., 11 Mar. 2006
2006/07		23 Oct., 17 Nov., 17 Dec. 2006, 4 Jan., 28 Feb., 25 Mar. 2007
2007/08	18 Nov. 2007	9 Nov., 13 Dec. 2007, 23 Jan., 29 Feb., 2 Mar. 2008
2008/09	8 Feb. 2009	19 Sep., 10 Oct., 4 Nov., 24 Dec. 2008, 6 Apr. 2009
2009/10		2 Sep., 4 Oct., 31 Oct., 14 Nov., 2 Dec., 16 Dec. 2009, 11 Feb., 7 Apr. 2010
2010/11		7 Sep., 11 Oct., 12 Nov., 19 Dec. 2010, 21 Feb., 10 Apr. 2011
2011/12		10 Sep., 5 Oct., 30 Oct., 27 Nov., 29 Dec. 2011, 7 Jan., 19 Feb., 13 Mar., 5 Apr. 2012

Table 4-2 Terra/ASTER image pairs used for the flow velocity measurements.

Period	Acquisition date		Interval (days)
	Master image	Slave image	
2002/03–2003/04	04 Nov. 2002	05 Nov. 2003	366
	04 Nov. 2002	02 Dec. 2003	393
	14 Mar. 2003	05 Nov. 2003	236
	14 Mar. 2003	02 Dec. 2003	263
2003/04–2004/05	05 Nov. 2003	27 Nov. 2004	388
	05 Nov. 2003	26 Jan. 2005	448
	02 Dec. 2003	27 Nov. 2004	361
	02 Dec. 2003	26 Jan. 2005	421
2004/05–2005/06	27 Nov. 2004	23 Dec. 2005	391
	27 Nov. 2004	11 Mar. 2006	469
	26 Jan. 2005	23 Dec. 2005	331
	26 Jan. 2005	11 Mar. 2006	409
2005/06–2006/07	12 Dec. 2005	17 Nov. 2006	340
	12 Dec. 2005	28 Feb. 2007	443
	11 Mar. 2006	17 Nov. 2006	251
	11 Mar. 2006	28 Feb. 2007	354
2006/07–2007/08	28 Feb. 2007	23 Jan. 2008	329
	28 Feb. 2007	29 Feb. 2008	366
2007/08–2008/09	13 Dec. 2007	10 Oct. 2008	302
	23 Jan. 2008	24 Dec. 2008	336
2008/09–2009/10	10 Oct. 2008	31 Oct. 2009	386
	10 Oct. 2008	16 Dec. 2009	432
	24 Dec. 2008	31 Oct. 2009	311
	24 Dec. 2008	19 Jan. 2010	391
2009/10–2010/11	31 Oct. 2009	02 Oct. 2010	336
	31 Oct. 2009	19 Dec. 2010	414
	31 Oct. 2009	05 Feb. 2011	462
	16 Dec. 2009	02 Oct. 2010	290
	16 Dec. 2009	19 Dec. 2010	368
	16 Dec. 2009	05 Feb. 2011	416
2010/11–2011/12	19 Jan. 2010	05 Feb. 2011	382
	02 Oct. 2010	05 Oct. 2011	368
	02 Oct. 2010	27 Nov. 2011	421
	02 Oct. 2010	25 Jan. 2012	480
	19 Dec. 2010	29 Dec. 2011	375
	19 Dec. 2010	07 Jan. 2012	384
	19 Dec. 2010	25 Jan. 2012	402
	05 Feb. 2011	29 Dec. 2011	327
	05 Feb. 2011	07 Jan. 2012	336
05 Feb. 2011	25 Jan. 2012	354	

Table 4-3 ALOS/PRISM stereo image pairs used for the DEM generation. B, N and F denote back, nadir and forward images.

Acquisition date	Mode	Scene ID
16 Nov. 2006	B, N	ALPSMB043205070 ALPSMN043205015
29 Nov. 2007	B, N, F	ALPSMB096885070 ALPSMN096885015 ALPSMF096884960
10 Nov. 2010	B, N	ALPSMB255445070 ALPSMN255445015

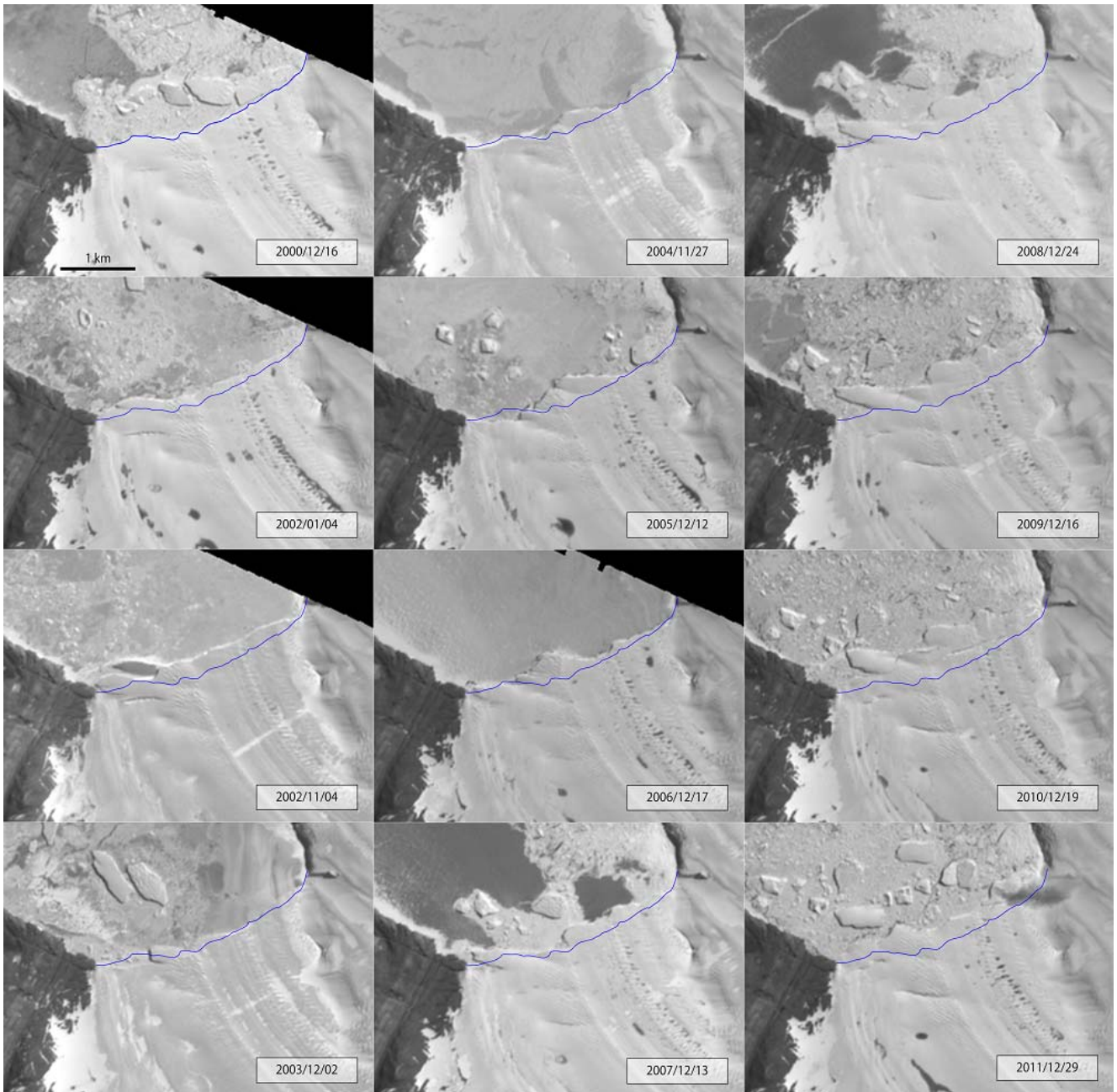


Fig. 4-1 Time-series imagery of the terminus from 2000/2001 to 2011/2012. These annual images are gray-scale-processed ASTER/VNIR images. Blue lines on the each image indicated the terminus position of 16th December, 2000.

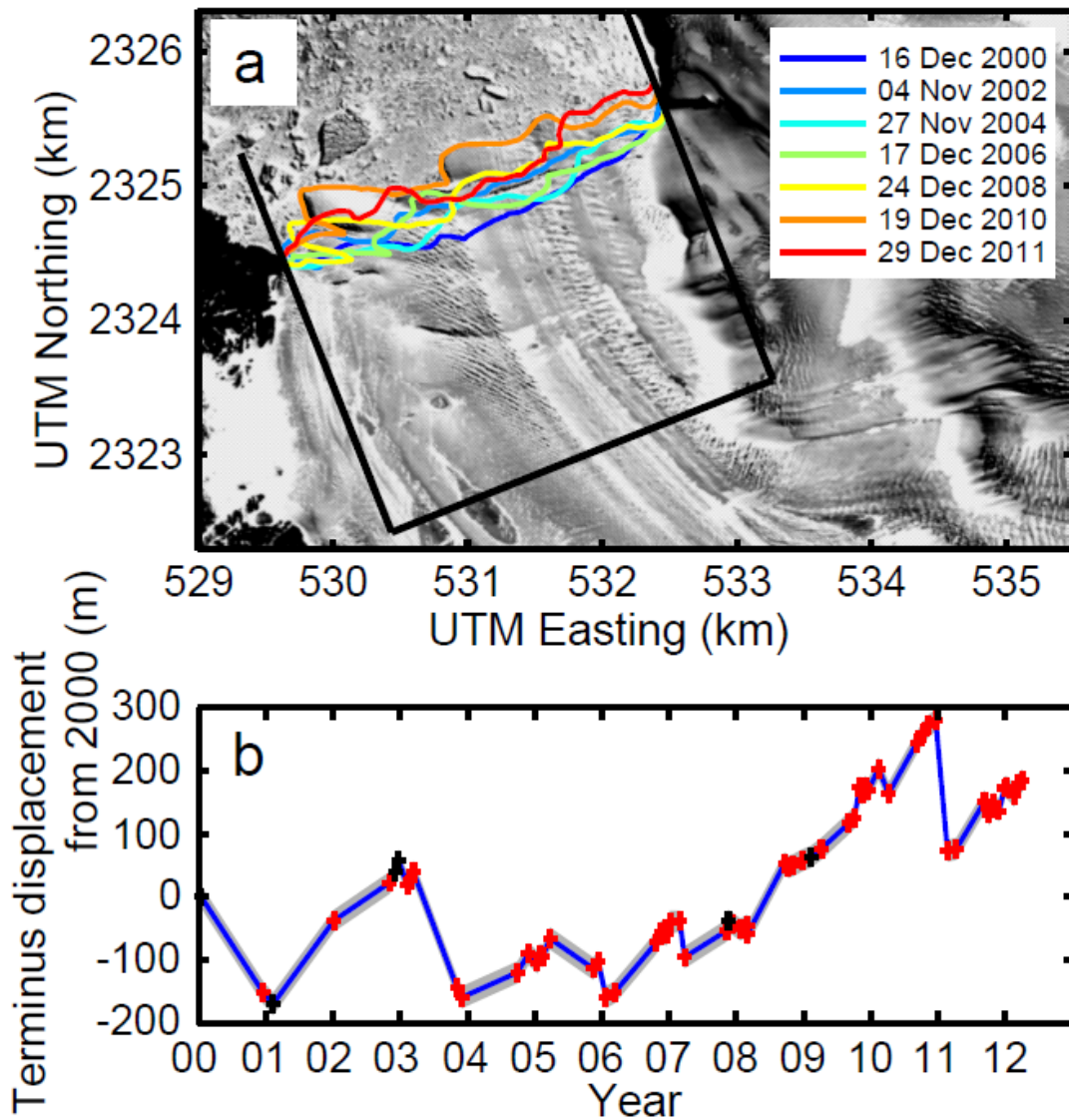


Fig. 4-2 (a) Glacier front positions from 2000–2011. Changes in the area delineated by the frontal margin and black lines are measured to compute mean terminus displacement. The background is an ALOS/PRISM image from 10th October, 2010. (b) Terminus displacement relative to the position in 2000. Data obtained from ASTER-VNIR and Landsat7/ETM are indicated by red and black crosses, respectively. Measurement error is indicated by the width of the grey line connecting the data points.

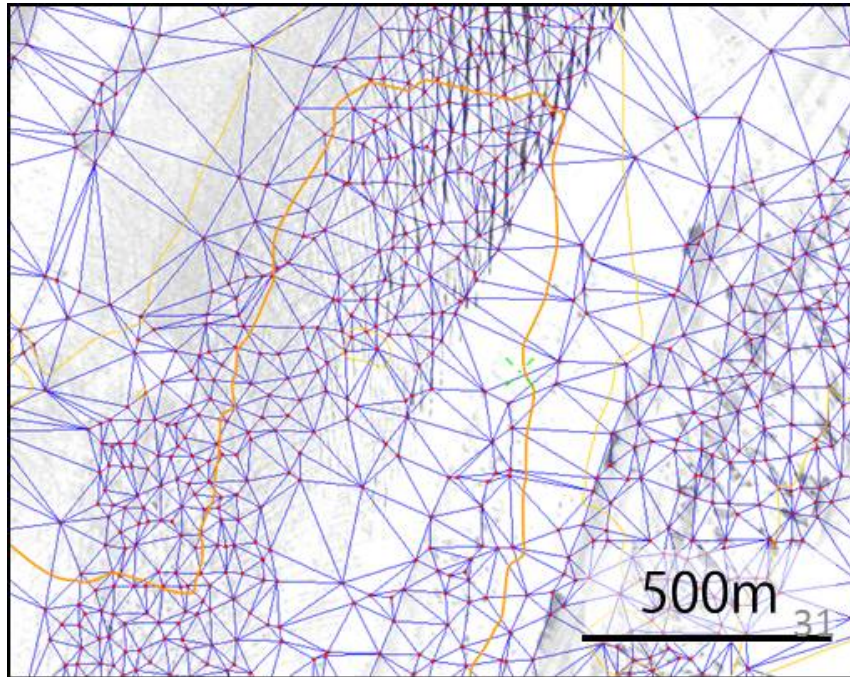


Fig. 4-3 A polygonal surface of the glacier generated with a digital photogrammetry system. The surface topography was expressed as triangulated irregular network (blue lines and red dots). Orange lines indicate elevation contour lines.

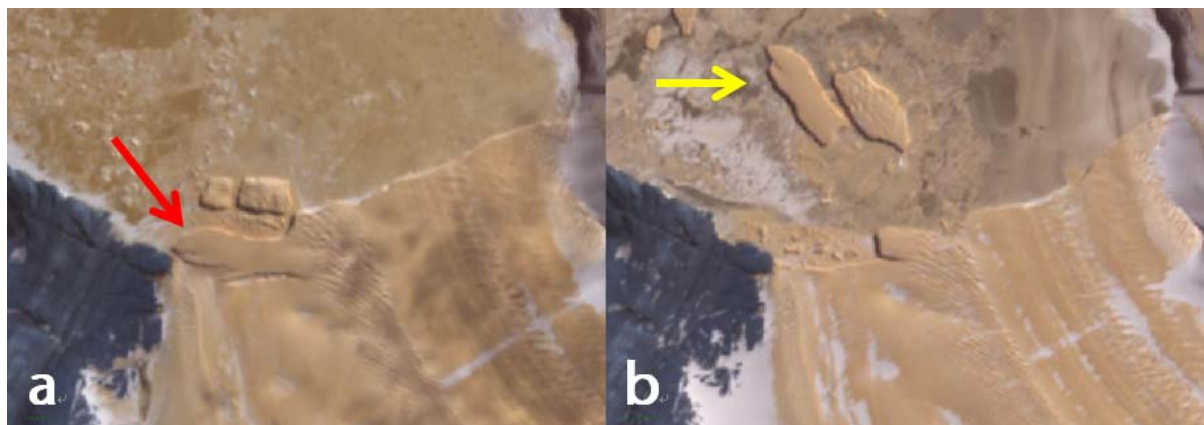


Fig. 4-4 The scenes of calving events in 2003. Red and yellow arrow indicated the calving region of the floating tongue and calved iceberg floating in front of the glacier, respectively. The ASTER/VNIR images captured (a) on 11st November, 2002 and (b) on 2nd December, 2003.

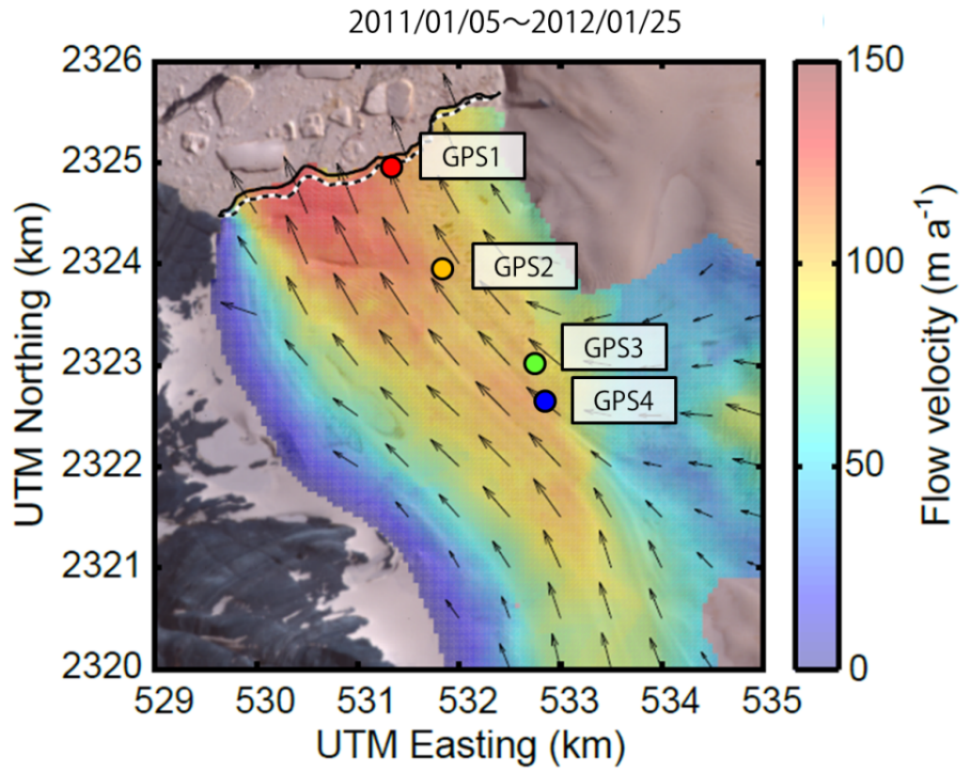


Fig. 4-5 Velocity vectors and horizontal velocity (color scale) between 5th January, 2011 and 24th January, 2012 obtained by the feature tracking analysis. Dashed and solid lines indicate the terminus positions on 5th January, 2011 and 24th January, 2012, respectively. The background is an ASTER image from 24th January, 2012.

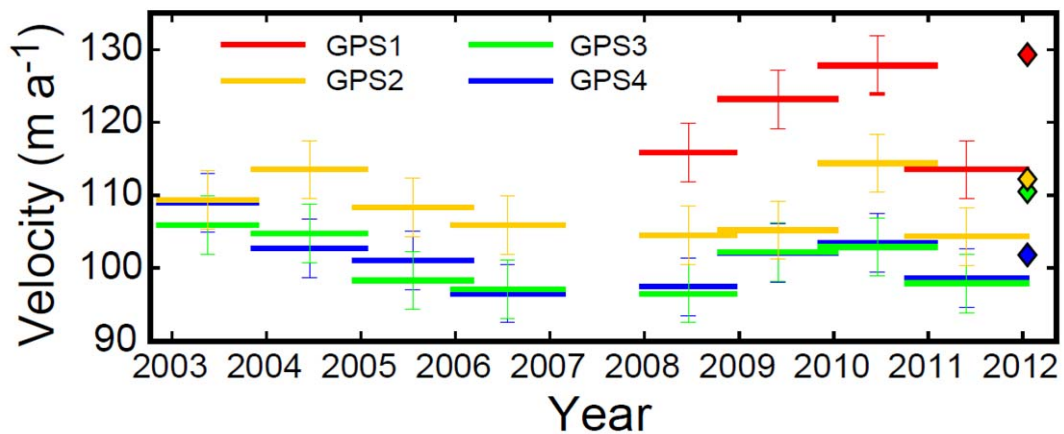


Fig. 4-6 Ice flow velocities at GPS1–4 from 2003 to 2012. The widths of the markers indicate the period of the COSI-Corr analysis. Data obtained by field GPS measurements are indicated by the diamonds.

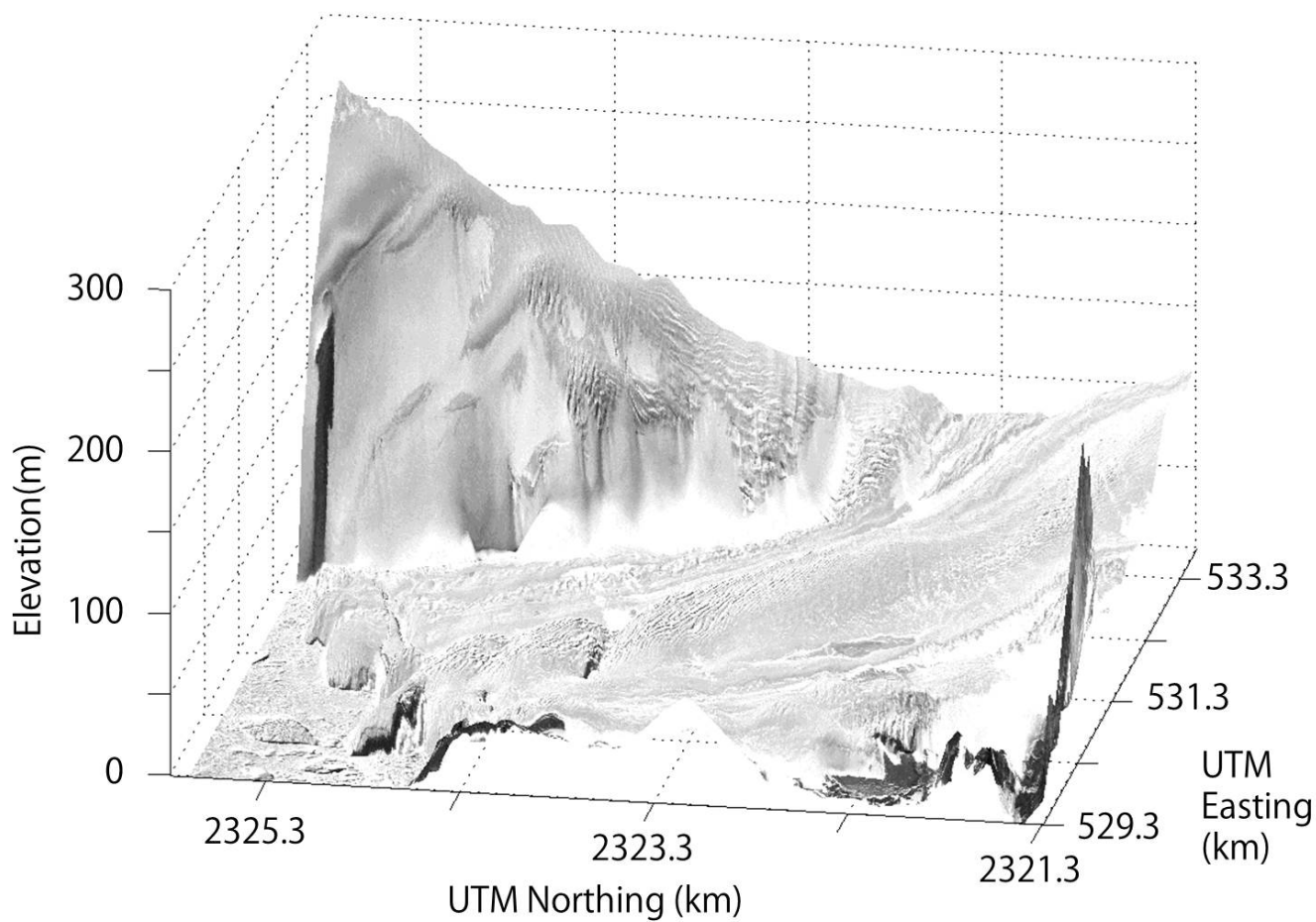


Fig. 4-7 An oblique view of surface topography of the Langhovde Glacier. The surface elevation is based on the DEM generated from ALOS/PRISM pair image captured on 17th November, 2007. The surface features are the PRISM image used for the DEM. The image is exaggerated to the vertical direction.

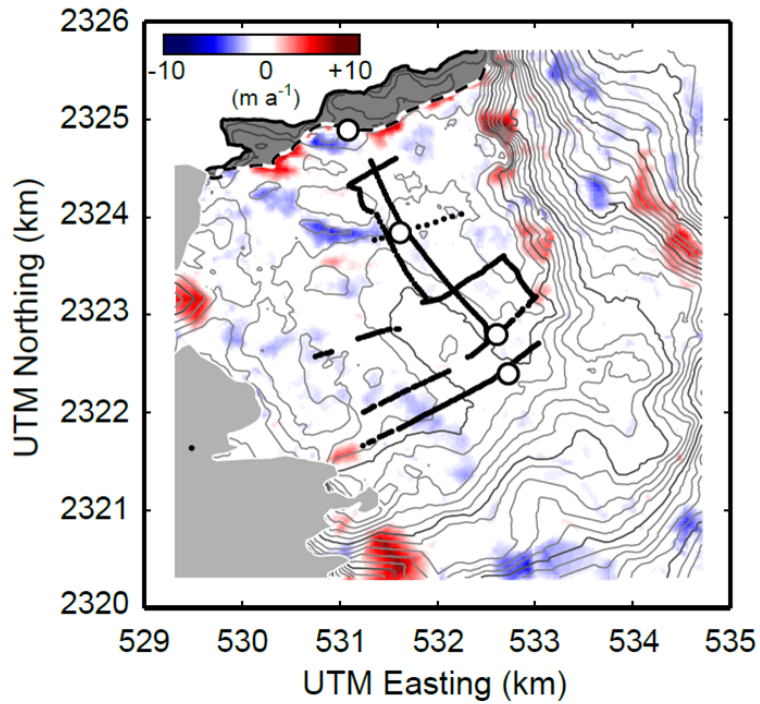


Fig. 4-8 Surface elevation change from 10th November, 2006 to 17th November, 2010. Bedrock is indicated by a grey color. The contour lines show surface elevation in 2010 with 10 m intervals. Dashed and solid lines indicate the terminus positions on 10th November, 2006 and 17th November, 2010, respectively.

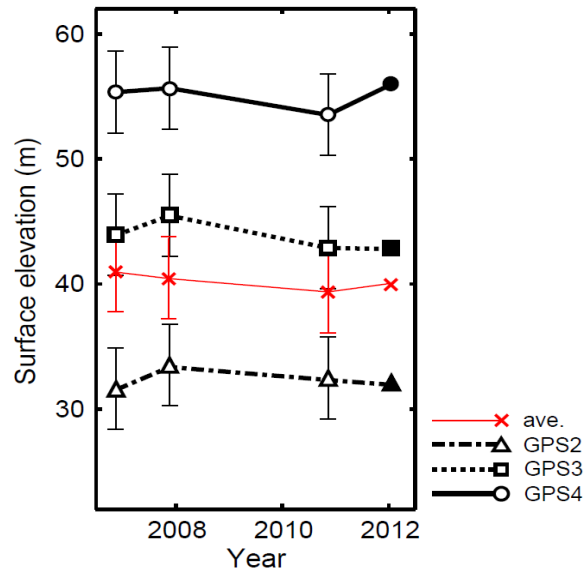


Fig. 4-9 Surface elevation at GPS2–4 and mean elevation along the GPS survey routes from 2006 to 2012. Data obtained by DEMs and field GPS surveys are indicated by the open and closed symbols, respectively.

## ***Chapter 5 Discussion***

### **5.1 Grounding line position**

Grounding line position is usually determined by surface observations as described in the introduction. However, our drilling confirmed that a shallow water layer penetrates upglacier from the grounding line estimated from a change in the surface slope. These results indicated the importance of field data for accurate determination of the grounding line position.

To further investigate the ice floating/grounding condition in the studied region, here we utilize ice thickness measured by the ice radar survey. We consider the hydrostatic equilibrium, which states the condition satisfies the balance of gravity and buoyancy force acting on floating ice (eq. 3-4). The thickness of ice slab floats on sea water can be estimated by based on Nye (1976).

$$T_{hydro} = \frac{\rho_w}{\rho_w - \rho_i} h, \quad (\text{eq. 5-1})$$

where  $T_{hydro}$  is ice thickness under the hydrostatic equilibrium,  $h$  is surface elevation above sea level, so called freeboard,  $\rho_i$  and  $\rho_w$  are ice and water densities as previously explained in chapter 3.3. This ice thickness estimated under the assumption of hydrostatic equilibrium is referred as  $T_{hydro}$ . We compare  $T_{hydro}$  with the ice thickness obtained by the ice radar measurement ( $T_{radar}$ ). When  $T_{hydro}$  agrees with  $T_{radar}$ , it suggests the ice satisfies the hydrostatic equilibrium and thus ice is most likely afloat. When  $T_{hydro}$  is greater than  $T_{radar}$ , ice is grounded on the bed. Similar analysis has been used in previous glacier studies. For example, ice floatation during the outburst event was analyzed in Gornergletscher (Sugiyama and others, 2008) and uplift of glacier terminus in a proglacial lake was investigated at Rhonegletscher (Tsutaki and others,

2013). For this analysis, we used ice thickness measured at 52 locations (Table 3-2), where return signals were clearly identified as described in chapter 3.2.5. Surface elevations at these ice radar measurement locations were results of GPS kinematic measurement (chapter 3.2.4).

Fig. 5-1 shows the glacier bed profiles estimated by  $T_{radar}$  and  $T_{hydro}$  along transverse ice radar profiles near the terminus, IR1 and IR2. Our GPS data clearly showed tidal vertical ice motion in these terminus regions. Thus, we assume that ice was afloat at every survey location along IR1 and IR2. In other words, we assume that hydrostatic equilibrium is satisfied along these two profiles.

Among these locations, there is discrepancy between  $T_{hydro}$  and  $T_{radar}$ . Because of the above assumption, this discrepancy can be attributed to the errors arise from uncertainties in ice radar data, surface elevation, and ice and seawater densities. The frequency distribution graph of the difference was illustrated in Fig. 5-2. According to the graph, a value of  $2\sigma$  (twice of standard deviation) is 54.6 m. Thus, we take 55 m as the upper limit of the difference expected for ice under floating condition (the hydrostatic equilibrium is satisfied), and assume that ice is grounded when  $T_{radar} - T_{hydro} > 55$  m. Otherwise ( $T_{radar} - T_{hydro} \leq 55$  m), we cannot distinguish that the measurement site was afloat or grounded. We applied this criterion to the  $T_{hydro}$  and  $T_{radar}$  obtained in the upper regions. The results at IR3, IR4 and IR5 are shown in Fig. 5-3. The measurement sites satisfied the grounding condition  $T_{radar} - T_{hydro} > 55$ m are distributed in the central part of IR3 and IR4, as well as in the western part near the glacier margin of IR5. These are regions where ice is probably grounded.

Fig. 5-4 shows the locations where ice is grounded or afloat according to the above criterion. At the central part of the glacier, grounded ice is observed

approximately within the glacier surface bump. Because freeboard is relatively large in this region, radar derived ice thickness is not thick enough to satisfy the hydrostatic equilibrium. Presumably, ice is grounded on a bedrock bump in this region, resulting in the relatively high ice surface elevation. The boundary of floating and grounding ice is generally in a good agreement with the grounding line estimated by the break in slope method. This is because the both methods rely on the surface topography. The break in slope method recognizes the change in the surface slope as the grounding line, and the hydrostatic equilibrium condition is violated immediately upglacier from this slope change.

Despite the agreement in these two methods, our borehole observations confirmed a thin subglacial water layer extends further upglacier (Fig. 5-4). Moreover, hydrostatic equilibrium condition was violated at the drilling sites as it is expected from ice mechanics (Fricker and Padman, 2006). Our field study demonstrated difficulties in accurate grounding line determination using only surface elevation data. Near the grounding line, force balance of glacier ice is influenced by longitudinal stresses exerted by neighboring ice. This results in violation of hydrostatic equilibrium even when water exists beneath a glacier. Particularly, bed geometry of the Langhovde Glacier is expected to be relatively complex, and this complexity enhances the difficulty in the grounding line estimation.

We argue that grounding line structure of a relatively small outlet glacier in Antarctica is not as simple as it has been often assumed. Further investigation of such structure is important because small outlet glaciers are abundant in East Antarctica and they discharge substantial amount of ice into the ocean by calving and subshelf melting.

## 5.2 Changes in the terminus position, velocity and surface elevation

Frontal variations of a calving glacier are often associated with ice velocity and ice thickness changes. Recent rapid retreat and thinning of tidewater glaciers in Greenland are thought to be related with ice acceleration. Detailed mechanisms are not well understood, but observations and numerical modelling works suggested that changes in the force balance near the calving front caused by glacier bed geometry plays a crucial role. Another example is tidewater and freshwater glaciers in the Patagonia Icefields. Some of the glaciers in Patagonia show rapid retreat or advance, which are not directly related to changes in climate. Recent rapid retreat of Glaciar Upsala is, for example, explained by acceleration occurred as a result of glacier terminus flotation (Sakakibara and others, 2013). The terminus got afloat because ice thinned at a region where bed is deepening upglacier.

To investigate the influence of ice dynamics and geometry changes on the frontal variations, we compare the terminus position, flow velocity and surface elevation over the period from 2003 to 2012 in Fig. 5-5. In addition to the observational data described before, the calving rate was calculated by subtracting the rate of the terminus displacement from the velocity near the glacier front.

$$C = v - \frac{dL}{dt} \quad (\text{eq. 5-2})$$

where  $C$  is the calving rate,  $L$  is the terminus position and  $t$  is time. The calving rates were calculated from annual flow velocity of the GPS1 near the terminus (see chapter 4.2) and the most retreated terminus position of a year. The calving rate was relatively constant at  $93 \text{ m a}^{-1}$  between 2003 and 2007, and it reduced to  $16 \text{ m a}^{-1}$  after 2008. Velocity increase was also observed from 2009 and 2010. Thus, the progressive advance from 2007 to 2011 was driven by a combination of ice velocity increase and calving rate

reduction. Two relatively large calving events occurred in 2003/2004 and 2011/2012, resulting in significant retreats of the terminus position. This observation indicates that the terminus position of the Langhovde Glacier is primarily controlled by sporadic large calving events, rather than changes in ice velocity. In addition to the importance of calving, detailed analysis shows changes in ice velocity also plays a role in the frontal variations.

Changes in the front position and ice speed often accompany ice thickness change. Nevertheless, the DEM analysis and GPS elevation survey in the field revealed that the mean change of surface elevation was only  $-1.6$  m ( $= -0.3$  m a<sup>-1</sup>) between 2006 and 2012. The magnitude of the elevation change was smaller than the DEM error ( $\pm 3.2$  m). Thus, in the case of the Langhovde Glacier, no significant ice thickness change occurred during the study period. Ice discharges by calving, surface ablation, basal and frontal melts are balanced by ice flow into the floating part of the glacier.

### 5.3 Driving mechanism of the changes in the calving rate

Our data demonstrated that sporadic large calving events control the glacier front position, thus it is crucial to understand the driving mechanism of calving at the Langhovde Glacier. The data show that calving occurs once every several years, but intervals of the events are not uniform. To find the mechanism controlling the calving intervals, we compare the calving record with climatic and sea ice conditions.

First, we compare the timing of the calving events with air temperature. The meteorological data including air temperature were measured at Syowa Station by the Japan Meteorological Agency since 1957. The meteorological observatory (69°00.3'S, 39°34.8'E, 18.4m a.s.l.) observed hourly air temperature, vapor pressure, relative humidity, wind speed and direction, amount of solar radiation precipitation and snow precipitation. In this study, we used monthly air temperature data from 2000 to 2012. The data are provided online in <http://www.data.jma.go.jp/obd/stats/etrn/index.php>.

The calving rate changed pronouncedly in 2008, however, the annual mean air temperature have no marked change in the studied period. The temperature trend at the Syowa Station was  $-0.078^{\circ}\text{C a}^{-1}$  from 2000 to 2012. Also, summer mean temperature (average of monthly mean air temperature in December, January and February) has the same tendency as the annual mean air temperature. Thus, it seems that there is no significant change in the calving rate over the studied period (Fig. 5-6). A coefficient of correlation between the calving rate and velocity change and the summer mean temperature is 0.15 and its p-value is 0.63 (Fig. 5-7). There is poor correlation between the calving rate and the summer temperature. The results indicated that the calving is not controlled by the air temperature.

Sea ice conditions in the Lützow-Holm Bay, where the Langhovde Glacier terminates, are possible drivers of the calving rate change. The sea ice cover in this region was relatively unstable (thin and low concentration) from the late 1990s to 2006. The sea ice disintegrated and flowed out from the bay in July 2006 (Ushio, 2006, 2010). After this event, heavy snow accumulation resulted in the formation of thick superimposed ice on newly formed sea ice, with the sea ice. Because relatively heavy snow fall condition lasts for several years, sea ice became thicker, producing a stable condition (Ushio, 2012). Recent snow fall increase in East Antarctica has also been reported by Gravity Recovery and Climate Experiment (GRACE) observations managed by National Aeronautics and Space Administration (NASA) and German Aerospace Center (DLR) (Borning and others, 2012).

Thus, we hypothesize that thick sea ice stabilized the glacier terminus, and inhibited a large calving event (Reeh and others, 2001). To investigate the influence of sea ice on the glacier calving, the sea ice concentration in the vicinity of the terminus of the Langhovde Glacier between from 2000 to 2012 was analyzed using satellite data. We used the data of Climate Data Record of Passive Microwave Sea Ice Concentration provided by National Snow and Ice Data Center (NSIDC) of National Ocean and Atmosphere Administration (NOAA). The sea ice concentration data were based on the data obtained by Scanning Multichannel Microwave Radiometer (SSMR) mounted on the satellite of NIMBUS-7 and Scanning Multichannel Microwave Radiometer (SSM/I) mounted on the DMSP 5D-2/F8, F11 and F13. The instruments measured surface/atmospheric microwave brightness temperatures at 6.63, 10.69, 18.0, 21.0, and 37.0 GHz (SSMR) and 19.35, 22.235, 37.0 and 85.5 GHz (SSM/I). The passive microwave signals were processed to produce sea ice concentration data sets (Meier and others, 2013, Peng and others, 2013). Daily and monthly data library of the sea ice concentration with 25 km spatial resolution is provided at the NSIDC (<http://nsidc.org/>

*data/seaice/pm.html*). The monthly sea ice concentration at 14 measurement points in Lützow-Holm Bay and their mean values were used in this analysis.

Fig. 5-8 shows variations of the sea ice concentration at 14 measurement point and their mean value. The sea ice concentration generally increased moderately from 2004 to 2010 and drops suddenly in 2011. It would appear that the large calving events in 2004 and 2011 occurred during a period of low sea ice concentration. Because weakening of sea ice during summer period is probably most relevant to calving, we focused on year to year variations of minimum values in the sea ice concentration which were most often recorded from January to March. Correlation coefficient between the minimum value of the sea ice concentration and the calving rate in that year is 0.39 and its p-value is 0.21 (Fig. 5-9).

This calculation reveals a relatively weak but significant positive correlation between calving rate and the sea ice concentration. Correlation of the calving rate with the sea ice concentration ( $R = 0.39$ ) is greater than that with summer temperature ( $R = 0.15$ ). It implies that the frequency of calving is influenced by the sea ice concentration.

Despite the fact that terminus position is primarily controlled by calving, ice flow velocity also plays a role as it is not constant over the study period. Flow velocities obtained by the satellite-based analysis in 2010/11 and 2011/12 were 8–10% smaller than those measured by the GPS field measurement in January 2012. This difference is greater than the measurement error. A possible interpretation for this sudden velocity change is a seasonal velocity variation. The satellite observations are made generally for periods spanning two summer seasons over winter, thus it represent approximately annual mean velocity. On the other hand, the field data was obtained within a summer season, and thus may have been influenced by seasonal velocity variation if it exists.

During the field campaign in 2012, penetration of surface melt water into the glacier bed was not observed in the region where ice is expected to be grounded. As such, it is not likely that surface melt water lubricated the bed and enhanced basal ice motion. We speculate that flow velocity increased during the summer under the influence of sea ice conditions in the Lützow-Holm Bay. Acceleration of calving glaciers due to the weakening of sea ice has been reported in Greenland (Amundson and others, 2010, Howat and others, 2010). Melting of sea ice in the Lützow-Holm Bay could have a similar effect on the flow velocity of the Langhovde Glacier.

Another possibility is that the relatively fast ice flow during the summer 2011/2012 was a result of the calving events in 2011/12. After the previous calving event in 2003/04, flow velocity increased in 2004. Such velocity change could be a glacier response to the loss of the glacier tongue.

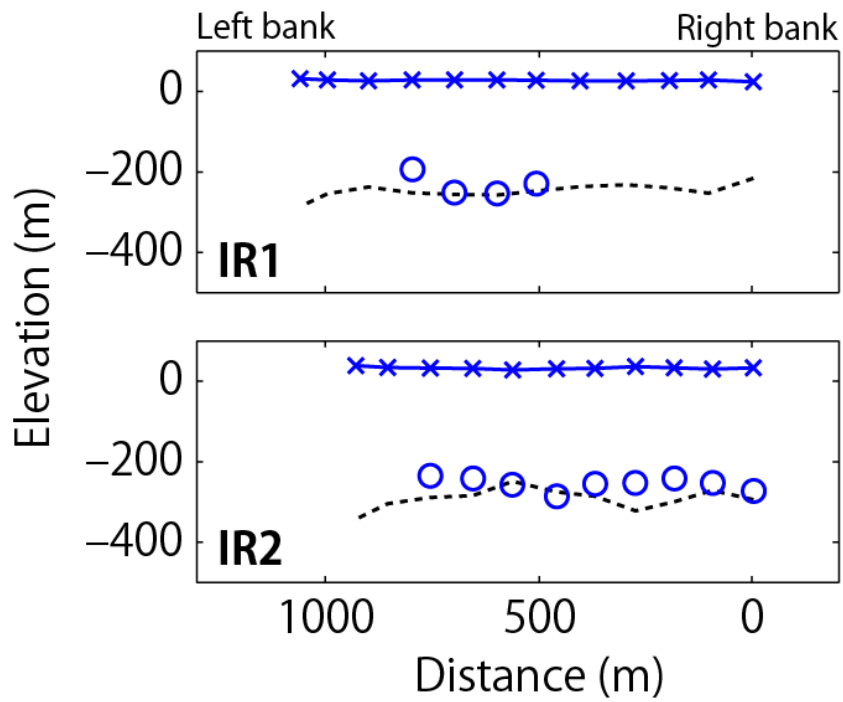


Fig. 5-1 Glacier surface elevation (blue line and  $\times$ ), bed elevation measured by the ice radar ( $T_{radar}$ , circles) and estimated by the hydrostatic equilibrium assumption ( $T_{hydro}$ , dotted line). The data are along IR1 and IR2, which were the two profiles nearest to the terminus.

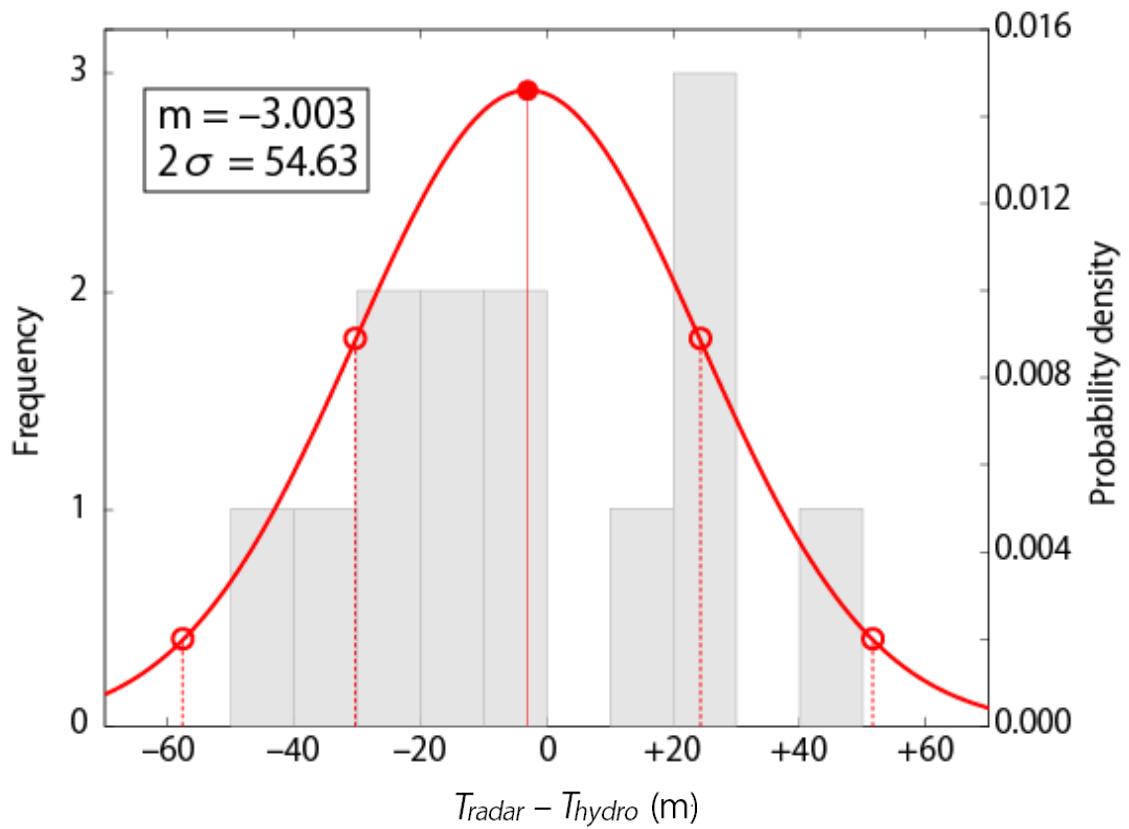


Fig. 5-2 Frequency distribution of  $T_{radar} - T_{hydro}$  in the IR1 and IR2 and normal distribution curve. Filled and open circle indicated mean value ( $m = -3.033$  m) and standard deviation  $\pm\sigma$  and  $\pm 2\sigma$  ( $2\sigma = 54.63$  m), respectively.

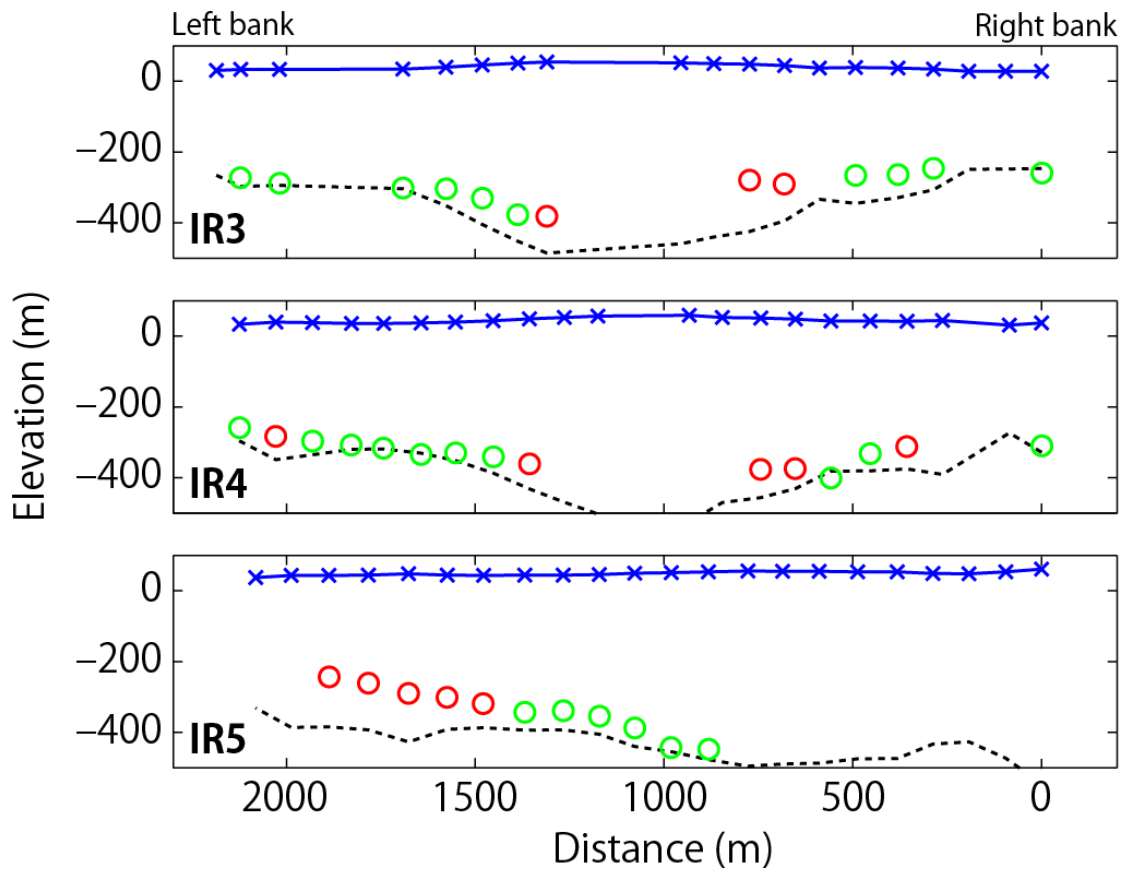


Fig. 5-3 Glacier surface elevation (blue line and  $\times$ ), bed elevation measured by the ice radar ( $T_{radar}$ , circles) and estimated by the hydrostatic equilibrium assumption ( $T_{hydro}$ , dotted line). The data are along IR3, IR4 and IR5. Red and green colors of the markers mean grounding and indecisive condition, respectively

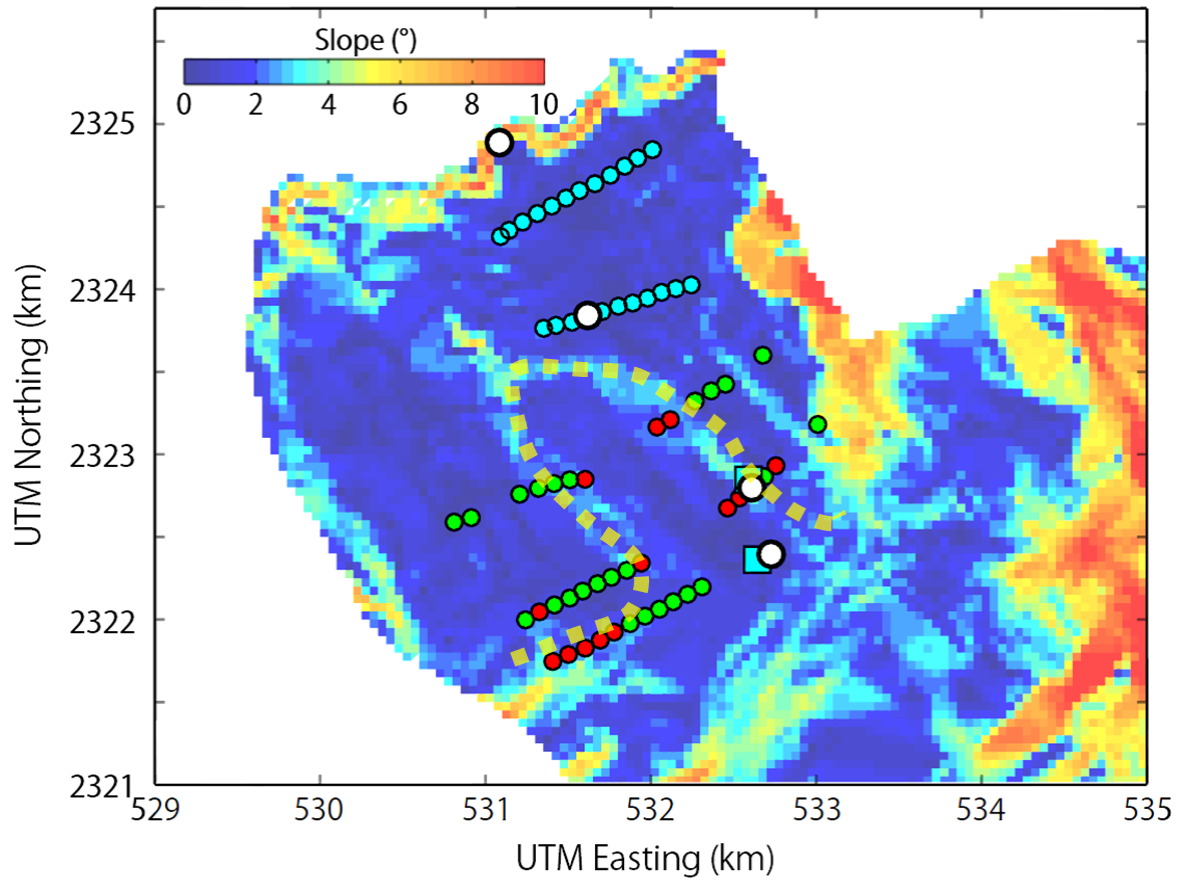


Fig. 5-4 Map showing the surface slope and subshelf condition in the terminus region. The colormap shows surface slope. Grounding line estimated by the break in slope method is indicated by the orange dotted line. The markers indicate the location of the ice radar survey sites (circle) and hot-water drilling sites (square). The colors of the markers show the subshelf condition; cyan, red and green indicate floating, grounding and ambiguous in this study, respectively.

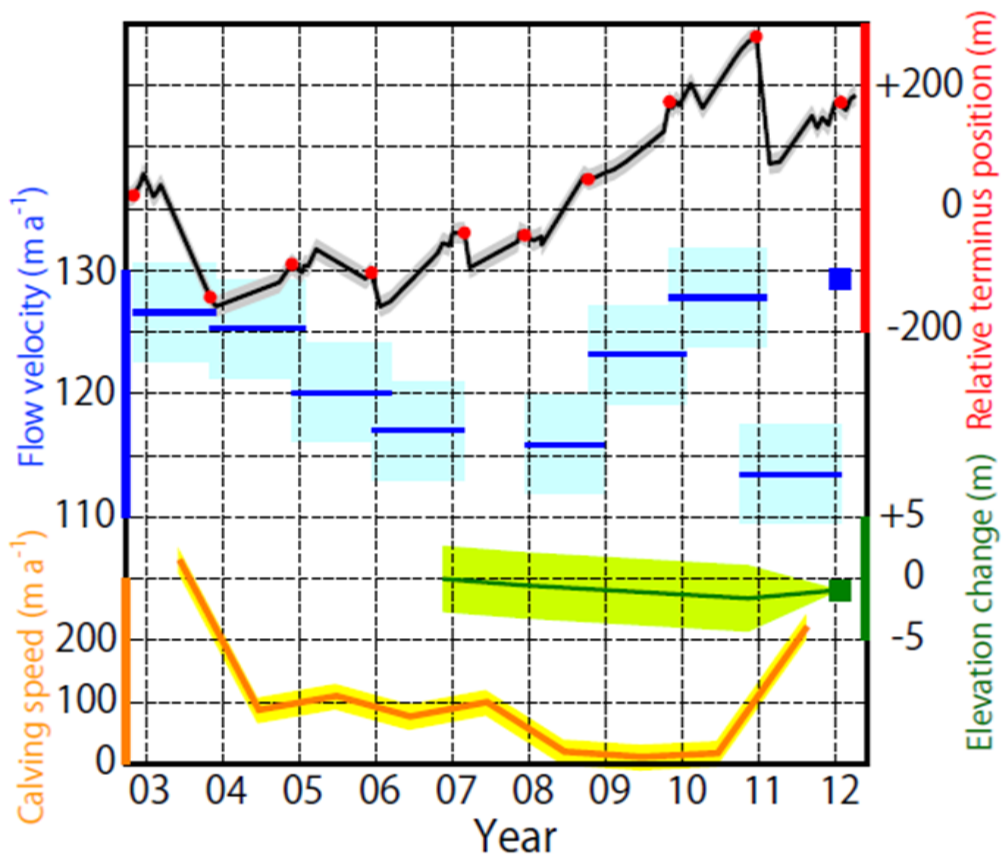


Fig. 5-5 Terminus displacement relative to 2000 (black line and red dots), flow velocity at GPS1 (blue line), mean surface elevation change along the GPS survey routes (green line) and calculated calving speed (yellow line) of the Langhovde Glacier from 2003–2012. The error ranges are indicated by shaded bands.

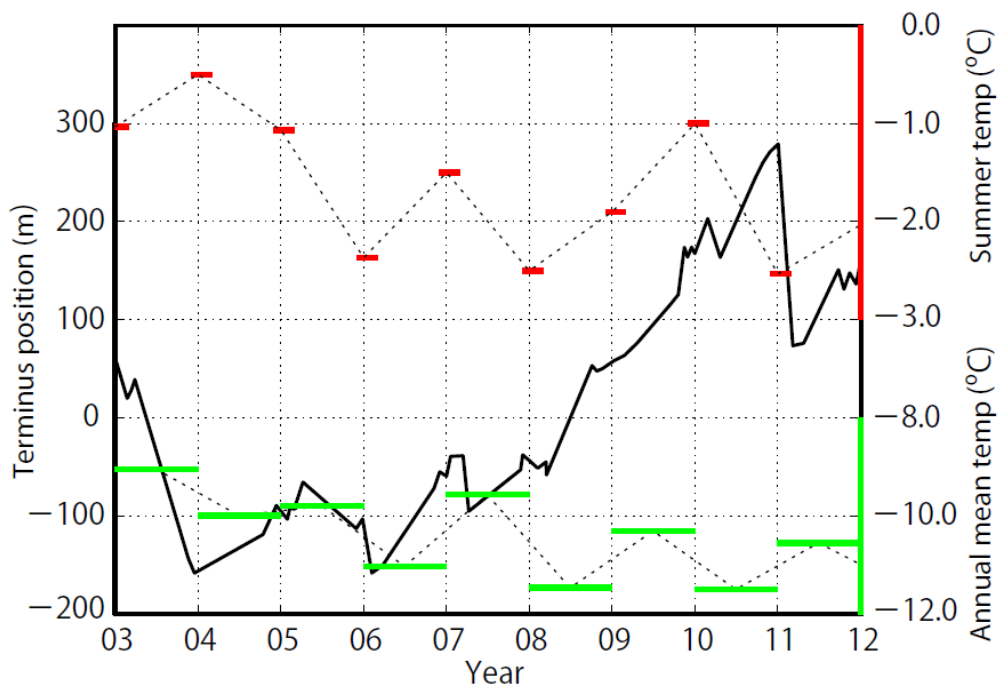


Fig. 5-6 Variations of terminus position (black) and mean temperature at Syowa Station. Red and green lines indicate annual mean and summer mean temperatures (average of monthly mean temperatures in December, January and February), respectively.

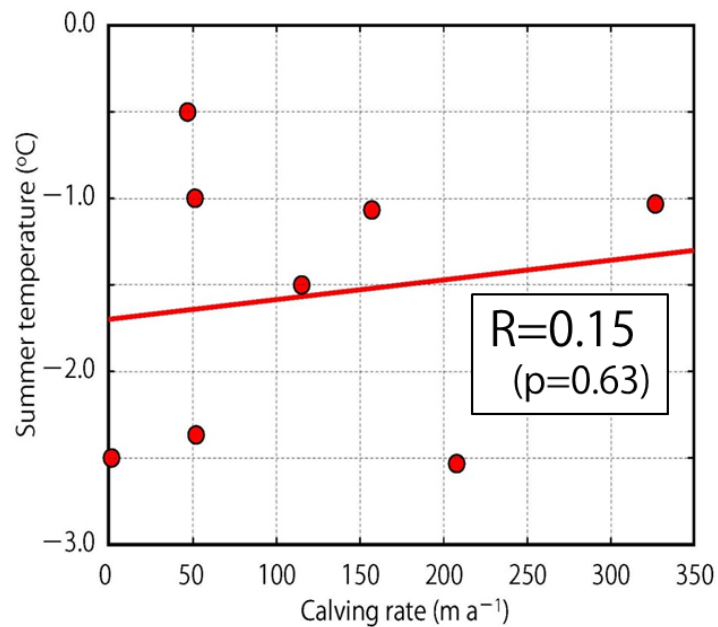


Fig. 5-7 A scatter plot of calving rate and summer mean temperature. The correlation coefficient  $R=0.15$  ( $p=0.63$ ).

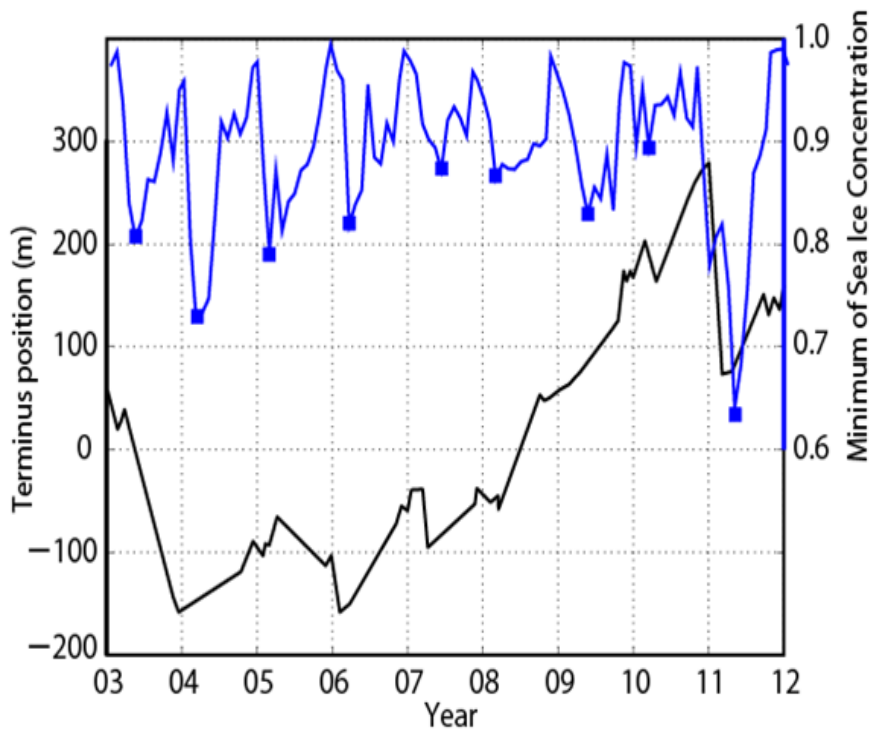


Fig. 5-8 Variations of terminus position (black) and minimum of sea ice concentration in Lützw-Holm Bay (blue).

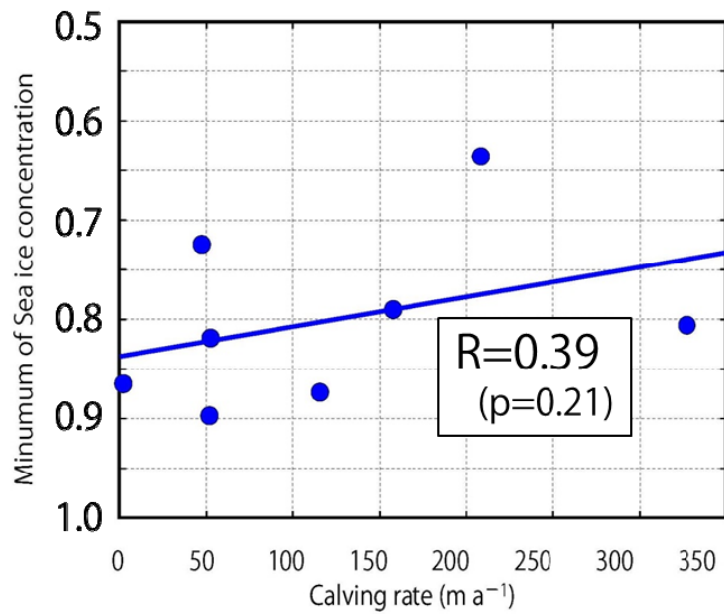


Fig. 5-9 A scatter plot of calving rate and minimum of sea ice concentration in Lützw-Holm Bay. The correlation coefficient  $R=0.39$  ( $p=0.21$ ).

## ***Chapter 6      Conclusions***

Antarctic ice sheet margins are rapidly changing in the recent years. Especially, changes in outlet glaciers and ice shelves, such as unexpected huge calving, drastic flow acceleration and significant ice thinning have been observed in West Antarctic ice sheet. A number of studies on these glaciers, mostly by means of remote sensing techniques, have causes and mechanism of these changes. Contrasting to the recently increasing numbers of reports in West Antarctica, studies of outlet glaciers in East Antarctica are relatively few. Several researches based on satellite-based analysis have been reported, but detailed field observations on the glaciers are very few. To better understand the cause and mechanisms of changes in outlet glaciers, we focused on the terminus changes, ice thickness and velocity variations of the Langhovde glacier, East Antarctica. We carried out satellite-based detailed studies for the period from 2000 to 2012, and combined the data with field measurements.

The field campaign on the glacier was conducted as a part of the JARE53 operation during Antarctic summer from 2011 to 2012. We carried out subglacial and englacial measurements using boreholes drilled with a hot-water drilling system. On the glacier, surface elevations and flow velocities were surveyed by GPS and ice thickness was measured using an ice radar system. The borehole observations indicated that ice was 398 m and 421 m thick at 2.8 km and 3.3 km from the terminus, respectively.

Borehole observations revealed a thin saline water column beneath the glacier, extending upstream from the grounding line estimated by a conventional method. Despite the existence of the saline water column at the drilling sites, ice does not satisfy the hydrostatic equilibrium. It was confirmed by these observations that our drilling sites were very close to the grounding line, but forms floating part of the glacier. The

results of the drilling and borehole measurements suggest that the structure of grounding line is more complex than it has been assumed. Most likely, complex bed geometry enhances the importance of longitudinal stresses conveyed from surrounding ice.

The surface elevation change from 2006 to 2012 was within 2.7 m. The small change in the elevation indicates a relatively stable condition during the study period, but the terminus position showed interesting variations within a limited distance. The terminus position of the Langhovde Glacier has been within a range of 450m between 2000 and 2012. Nevertheless, the terminus position showed complex variations under the influence of calving events and ice velocity changes during the period. The glacier progressively advanced by 380 m from January 2007 to January 2010. The velocity gradually decreased from 2003/2004 to 2008/2009, and then it increased by  $9.9 \text{ m a}^{-1}$  from 2008/2009 to 2010/2011. It seems that the changes in the terminus position are influenced by flow velocity because these changes occurred during the same period. However, the observed advance was not due to a flow velocity change, but more influenced by the reduction in the calving rate in 2007. After the detailed analysis of satellite data, frontal variations of the Langhovde Glacier are primarily controlled by sporadic large calving events, which mean changes in the calving rate.

To better understand the cause of the large calving, we compared the calving rate with air temperature recorded at Syowa Station, and with the sea ice concentration in front of the glacier which based on satellite data. There is no clear trend in the annual mean temperature record during the study period, and thus no correlation was found between the calving rate and the summer temperature. On the other hand, we found that discharge of sea ice out of Lützow-Holm Bay in the summer of 2006 was related to the increase in the calving rate. Moreover, reduction in the calving rate in 2008–2011

coincided with the formation of thick sea ice caused by heavy snow fall during this period. These data suggest that the calving rate of the Langhovde Glacier is affected by the sea ice condition in the ocean. Thinning or thickening of sea ice in front of outlet glaciers has a potential to drive rapid advance and retreat of glacier front.

It is still under question if sea ice concentration controls the changes in flow velocity. In our data, sea ice and velocity have changed during the same period, but their relationship is not very clear. Because ice velocity is important for terminus position and ice discharge into the ocean, more effort is needed to understand the impact of sea ice change to the variations of outlet glaciers.



## *Acknowledgements*

This doctoral study was guided by Dr. Shin Sugiyama (Hokkaido University) as a doctoral adviser. He offered opportunities, materials and instructions required to carry out my graduate study for the last 6 years since the beginning of the master program. I would like to express my gratitude to him for valuable advice and continuous support to me.

Professor Ralf Greve (Hokkaido University) acted as a chief of the committee for the evaluation of this Ph.D. thesis. As a leader of the research group, he has provided me constructive comments and suggestion during the research activity in the Glacier and Ice Sheet Research Group. Professor Kay I. Ohshima (Hokkaido University), Dr. Takanobu Sawagaki (Hokkaido University) and Professor Hideaki Motoyama (National Institute of Polar Research), committee members, provided instructive comments and generous support for the study.

The field campaign on the Langhovde Glacier was a part of the research program of the JARE 53. This research project was led by Dr. Shin Sugiyama with collaboration with Dr. Shigeru Aoki (Hokkaido University), Professor Satoshi Imura (National Institute of Polar Research), Dr. Takanobu Sawagaki, Mr. Kunio Shinbori (Hokkaido University), Dr. Masato Furuya (Hokkaido University), Professor Takashi Saitoh (Kyoto University), Dr. Tsutomu Yamanokuchi (Remote Sensing Technology Center of Japan) and Dr. Kazuki Nakamura (Nihon University). Contributions of the above members to the project were greatly acknowledged.

Our field activity in Antarctica was supported by JARE 53 and JARE 52. The success of the field campaign was only possible with materials and technical support of

the JARE members. I would like to thank Professor Hisao Yamagishi (National Institute of Polar Research) and Mr. Kenji Ishizawa (National Institute of Polar Research) as leaders of JARE 53, all member of the expedition team and sailors of ice breaker Shirase for helping us in the field.

Special thanks to Mr. Kazuo Higuchi (National Institute of Polar Research) and Mr. Wataru Nara (Nomad) as field assistant, Mr. Masanori Shirahama (Isuzu motors) as a mechanic and Dr. Daisuke Shimizu (Hokkaido University), Mr. Noriaki Izumi (Japan Coast Guard), Ms. Fuko Sugimoto (Hokkaido University), Dr. Yukiko Tanabe (Japan Society for the Promotion of Science), Dr. Hideo Akiyoshi (Shimane University), Mr. Makoto Hori (The University of Tokyo), Mr. Satoshi Onoguchi (Sendai High School), Mr. Kazunobu Shinotsuka (Dynac) and Mr. Chusaku Ikeda (Tsukuba University) who carried out the field research on the glacier and helping us. During the research activity on the glacier, Dr. Shin Sugiyama and Dr. Takanobu Sawagaki instructed me on my research skills. I am most grateful for their carefully guidance in the field.

A part of the satellite images used for the analysis was provided by Dr. Kazuki Nakamura. Dr. Takanobu sawagaki and Dr. Tsutomu Yamanokuchi instructed me how to process the images, and give me valuable advices over the course of the study. I would like to thank them for their cooperation and constructive comments on the study. I would like to thank all the members of the Glacier and Ice Sheet Research Group, Institute of Low Temperature Science, Hokkaido University for their kind support during my doctoral study as a member of the group.

This research was carried out as a part of the JARE53 program. Financial support was provided from the National Institute of Polar Research. The project was also financially supported by Grant-in-Aid for Challenging Exploratory Research <KAKENHI>, 23651002, 2011-2014, funded by the Japanese Ministry of Education, Culture, Sports, Science and Technology and Japan Society for the Promotion of Science. Additionally, travel expenses for Antarctica and an international conference were supported by Research Grant of Japan Polar Research Association and Global COE program of Hokkaido University.

February, 2014

Takehiro Fukuda



## References

- Amundson J.M., M. Fahnestock, M. Truffer, J. Brown, M.P. Luthi, and R.J. Motyka. 2010. Ice melange dynamics and implications for terminus stability, Jakobshavn Isbre, Greenland. *Journal of Geophysical Research - Earth Surface*, **115**(F1), F01005. doi: 10.1029/2009JF001405.
- Aoki, S., T. Ozawa, K. Doi, and K. Shibuya. 2000. GPS observation of the sea level variation in Lützow-Holm Bay, Antarctica. *Geophysical Research Letters*, **27**(15), 2285–2288. doi: 10.1029/1999GL011304.
- Berthier, E., T.A. Scambos, and C.A. Shuman. 2012. Mass loss of Larsen B tributary glaciers (Antarctic Peninsula) unabated since 2002. *Geophysical Research Letters*, **39**(13), L13501. doi: 10.1029/2012GL051755.
- Bindschadler, R., P. Vornberger, A. Fleming, A. Fox, J. Mullins, D. Binnie, S. J. Paulsen, B. Granneman, and D. Gorodetzky. 2008. The Landsat Image Mosaic of Antarctica. *Remote Sensing of the Environment*, **112**, 4214–4226. doi: 10.1016/j.rse.2008.07.006.
- Berthier, E., T. A. Scambos, and C. A. Shuman. 2012. Mass loss of Larsen B tributary glaciers (Antarctic Peninsula) unabated since 2002. *Geophysical Research Letters*, **39**(13). doi: 10.1029/2012GL051755.
- Brunt, K. M., H. A. Fricker, L. Padman, and S. O'Neel. 2010. *ICESat-Derived Grounding Zone for Antarctic Ice Shelves*. Boulder, Colorado USA: National Snow and Ice Data Center. doi: 10.7265/N5CF9N19.
- Boening, C., M. Lebsock, F. Landerer, and G. Stephens. 2012. Snowfall–drive mass change on the East Antarctic ice sheet. *Geophysical Research Letters*, **39**(21), L21501. doi: 10.1029/2012GL053316.
- Cogley, J.G. 2009. A more complete version of the World Glacier Inventory. *Annals of Glaciology*, **50**, 32–38. doi: 10.3189/172756410790595859.

- Cook, A.J. and D.G. Vaughan. 2010. Overview of areal changes of the ice shelves on the Antarctic Peninsula over the past 50 years. *The Cryosphere*, **4**(1), 77–98. doi: 10.5194/tc-4-77-2010.
- Depoorter, M. A., J. L. Bamber, J. A. Griggs, J. T. M. Lenaerts, S. R. M. Ligtenberg, M. R. van den Broeke, and G. Moholdt. 2013. Calving fluxes and basal melt rates of Antarctic ice shelves. *Nature*, **502**(580), 89–92. doi: 10.1038/nature12737.
- Drewry, D. J. 1983. *Antarctica: Glaciological and Geophysical Folio*. Scott Polar Research Institute, University of Cambridge.
- Fox, A. J., and D. G. Vaughan. 2005. The retreat of Jones Ice Shelf, Antarctic Peninsula. *Journal of Glaciology*, **51**(175), 555–560. doi: 10.3189/172756505781829043.
- Fretwell, P., H.D. Pritchard, D.G. Vaughan, J.L. Bamber, N.E. Barrand, R. Bell, C. Bianchi, R.G. Bingham, D.D. Blankenship, G. Casassa, G. Catania, D. Callens, H. Conway, A.J. Cook, H.F.J. Corr, D. Damaske, V. Damm, F. Ferraccioli, R. Forsberg, S. Fujita, P. Gogineni, J.A. Griggs, R.C.A. Hindmarsh, P. Holmlund, J.W. Holt, R.W. Jacobel, A. Jenkins, W. Jokat, T. Jordan, E.C. King, J. Kohler, W. Krabill, M. Riger-Kusk, K.A. Langley, G. Leitchenkov, C. Leuschen, B.P. Luyendyk, K. Matsuoka, Y. Nogi, O.A. Nost, S.V. Popov, E. Rignot, D.M. Rippin, A. Riviera, J. Roberts, N. Ross, M.J. Siegert, A.M. Smith, D. Steinhage, M. Studinger, B. Sun, B.K. Tinto, B.C. Welch, D.A. Young, C. Xiangbin, and A. Zirizzotti. 2013. Bedmap2: improved ice bed, surface and thickness datasets for Antarctica. *Cryosphere*, **7**, 375–393. doi: 10.5194/tc-7-375-2013.
- Fricker, H. A., I. Allison, M. Craven, G. Hyland, A. Ruddell, N. W. Young, R. Coleman, M. King, K. Krebs, and S. Popov. 2002. Redefinition of the Amery Ice Shelf, East Antarctica, grounding zone. *Journal of Geophysical Research - Solid Earth*, **107**(B5). doi: 10.1029/2001JB000383.
- Fricker, H.A., and L. Padman. 2006. Ice shelf grounding zone structure from ICESat laser altimetry. *Geophysical Research Letters*, **33**, L15502. doi: 10.1029/

2006gl026907.

- Fujiwara, K. 1971. Soundings and submarine topography of the glaciated continental shelf in Lützow -Holm Bay, East Antarctica. *Reports of the Japanese Antarctic Research Expedition*, **41**, 81–103.
- Fukuda T., S. Sugiyama, S. Matoba and T. Shiraiwa. 2011. Glacier flow measurement and radio-echo sounding at Aurora Peak, Alaska, in 2008. *Annals of Glaciology*, **52** (58), 49–54. doi: 10.3189/172756411797252130.
- Goldstein, R. M., H. Engelhardt, B. Kamb, and R. M. Frolich. 1993. Satellite Radar Interferometry for Monitoring Ice Sheet Motion: Application to an Antarctic Ice Stream. *Science*, **262**(5139), 1525–1530. doi: 10.1126/science.262.5139.1525.
- Gow, A.J. 1970. Preliminary results of studies of ice cores from the 2164 m deep drill hole, Byrd Station, Antarctica. *International Association of Scientific Hydrology*, **86**, 78–90.
- Greve, R., and H. Blatter. 2009. *Dynamics of Ice Sheets and Glaciers*. Springer. doi:10.1007/978-3-642-03415-2.
- Harada, N., N. Handa, M. Fukuchi, and R. Ishiwatari. 1995. Hydrocarbon record of a marine sediment core from Lützow-Holm Bay, Antarctica. *Proceedings of the NIPR Symposium on Polar Biology*, **8**, 163–176.
- Herman, F., B. Anderson, and S. Leprince. 2011. Mountain glacier velocity variation during a retreat/advance cycle quantified using sub-pixel analysis of ASTER images. *Journal of Glaciology*, **57**(202), 197–207. doi: 10.3189/002214311796405942.
- Horgan, H. J. and S. Anandkrishnan. 2006. Static grounding lines and dynamic ice streams: Evidence from the Siple Coast, West Antarctica. *Geophysical Research Letters*, **33**(18), L18502. doi: 10.1029/2006GL027091.
- Howat, I.M., J.E. Box, Y. Ahn, A. Herrington, and E.M. McFadden. 2010. Seasonal variability in the dynamics of marine-terminating outlet glaciers in Greenland.

- Journal of Glaciology*, **56**(198), 601–613. doi: 10.3189/002214310793146232.
- Intergovernmental Panel on Climate Change (IPCC). 2013. IPCC Fifth Assessment Report - Observations: Cryosphere, 317–382.
- Joughin, I., E. Rignot, C. E. Rosanova, B. K. Lucchitta, and J. Bohlander. 2003. Timing of recent accelerations of Pine Island Glacier, Antarctica. *Geophysical Research Letters*, **30**(13), 1706. doi: 10.1029/2003GL017609.
- Kamimura, K. and K. Shibuya. 1983. Geophysical investigation in the eastern part of Lützow-Holm bay, Antarctica. *Antarctic Earth Science Forth international symposium*, 519–521.
- Kanda, H. 1986. Moss communities in some ice-free areas along the Soya Coast, East Antarctica. *Memories of National Institute for Polar Research*, Special Issue, **44**, 229–240.
- Kawamura, T., K. I. Ohshima, T. Takizawa, and S. Ushio. 1997. Physical, structural, and isotopic characteristics and growth processes of fast sea ice in Lützow-Holm Bay, Antarctica. *Journal of Geophysical Research*, **102**, 3345–3355. doi: 10.1029/96JC03206.
- Komazawa, K., and T. Sawagaki. 2013. Detection of the marginal fluctuation of the Antarctic ice sheet by multi-temporal remote sensing stereo images in the vicinity of the Syowa Station. *Summaries of JSSI & JSSE Joint Conference on Snow and Ice Research- 2013/Kitami*, The Japanese Society of Snow and Ice, 160.
- Kudoh S., Y. Tanabe, T. Inoue, S. Imura, and H. Kanda. 2009. Breaching of a perennial snow dam below Lake Hyoga Ike in the Langhovde region of the S&ocirc;ya Coast, East Antarctica: Probable effect of disturbance events on the distribution and colonization of flora within/around the lake. *Antarctic record*, **53**(1), 114–122.
- Lamsal, D., T. Sawagaki, and T. Watanabe. 2011. Digital terrain modeling using Corona

- and ALOS PRISM data to investigate the distal part of Imja Glacier, Khumbu Himal, Nepal. *Journal of Mountain Science*, **8**(3), 390–402. doi: 10.1007/s11629-011-2064-0.
- Lee, H., C. K. Shum, I. M. Howat, A. Monaghan, Y. Ahn, J. Duan, J. Guo, C. Kuo, and L. Wang. 2012. Continuously accelerating ice loss over Amundsen Sea catchment, West Antarctica, revealed by integrating altimetry and GRACE data. *Earth and Planetary Science Letters*, **321-322**, 74–80. doi: 10.1016/j.epsl.2011.12.040.
- Leprince, S., S. Barbot, F. Ayoub, and J.P. Avouac. 2007. Automatic and precise orthorectification, coregistration, and subpixel correlation of satellite images, application to ground deformation measurements. *Institute of Electrical and Electronics Engineers (IEEE) Transaction of Geoscience and Remote Sensing*, **45**(6), 1529–1558. doi: 10.1109/TGRS.2006.888937.
- Lewis, E.L. 1980. The Practical Salinity Scale 1978 and its antecedents. *IEEE Journal of Oceanic Engineering*, **OE-5**(1), 3–8. doi: 10.1109/JOE.1980.1145448.
- Lipps, J. H., T. E. Ronan Jr., and T. E. Delaca. 1979. Life below the Ross Ice Shelf. *Science*, **203**, 447–449. doi: 10.1126/science.203.4379.447.
- MacGregor, J. A., G. A. Catania, M. S. Markowski, and A. G. Andrews. 2012. Widespread rifting and retreat of ice-shelf margins in the eastern Amundsen Sea Embayment between 1972 and 2011. *Journal of Glaciology*, **58**(209), 458–466. doi: 10.3189/2012JoG11J262.
- Marzeion, B., A.H. Jarosch, and M. Hofer. 2012. Past and future sea-level change from the surface mass balance of glaciers. *Cryosphere*, **6**, 1295–1322. doi: 10.5194/tc-6-1295-2012.
- Massom, R. A. 2003. Recent iceberg calving events in the Ninnis Glacier region, East Antarctica. *Antarctic Science*, **15**(2), 303–313. doi: 10.1017/S0954102003001299.

- Matsuoka, K., S. Horikawa, T. Shiraiwa, Y.D. Muravyev, A.N. Salamatin, A.A. Ovsyannikov, H. Maeno, and M. Ohi. 1999. Radio echo sounding at the summit ice cap of the Ushkovsky volcano, Kamchatka. *Cryospheric Studies in Kamchatka II*, 20-24.
- Matsumoto, Y., M., Yoshida, and K. Yanai. 1979. Geology and geologic structure of the Langhovde and Skarvsnes regions, East Antarctica. *Memories of National Institute for Polar Research*, Special Issue, **14**, 106–120.
- Meier, M. F., M. B. Dyurgerov, U. K. Rick, S. O'Neel, W. T. Pfeffer, R. S. Anderson, S. P. Anderson, and A. F. Glazovsky. 2007. Glaciers Dominate Eustatic Sea-Level Rise in the 21st Century, *Science*, **317**, 1064–1067, doi: 10.1126/science.1143906.
- Meier, W., F. Fetterer, M. Savoie, S. Mallory, R. Duerr, and J. Stroeve. 2013. *NOAA/NSIDC Climate Data Record of Passive Microwave Sea Ice Concentration*. Boulder, Colorado USA: National Snow and Ice Data Center. doi: 10.7265/N55M63M1.
- Miles, B.W.J., C.R. Stokes, A. Vieli and N.J. Cox. 2013. Rapid, climate-driven changes in outlet glaciers on the Pacific coast of East Antarctica. *Nature*, 500, 563–566. doi:10.1038/nature12382.
- Moon, T., and I. Joughin. 2008. Changes in ice front position on Greenland's outlet glaciers from 1992 to 2007. *Journal of Geophysical Research: Earth Surface*, **113**, F02022. doi: 10.1029/2007JF000927.
- Nogi, Y., W. Jokat, K. Kitada, and D. Steinhage. 2013. Geological structures inferred from airborne geophysical surveys around Lützow-Holm Bay, East Antarctica. *Precambrian Research*, **234**, 279–287. doi: 10.1016/j.precamres.2013.02.008.
- Nye, J.F. 1976. Water flow in glaciers: Jokulhlaups, tunnels, and veins. *Journal of Glaciology*, **17**(76), 181–207.
- Ohshima K.I., and T. Kawamura. 1994. Oceanographic Data in Lützow-Holm Bay of

- the Antarctic Climate Research Program from January 1991 to February 1992 (JARE-32). *JARE Data Reports, Oceanography*, **15**, 1–35.
- Ohshima, K. I., T. Takizawa, S. Ushio, and T. Kawamura. 1996. Seasonal variations of the Antarctic coastal ocean in the vicinity of Lützow-Holm Bay. *Journal of Geophysical Research: Oceans*, **101**(C9), 20617–20628. doi: 10.1029/96JC01752.
- Ohtani, S., H. Kanda, and Y. Ino. 1990. Microclimate data measured at the Yukidori Valley, Langhovde, Antarctica in 1988–1989. *JARE Data Reports*, **152** (Terrestrial Biology 1), 216.
- Peng, G., W. Meier, D. Scott, and M. Savoie. 2013. A long-term and reproducible passive microwave sea ice concentration data record for climate studies and monitoring. *Earth System Science Data*, **5**, 311–318. doi: 10.5194/essd-5-311-2013.
- Pritchard, H. D., S. R. M. Ligtenberg, H. A. Fricker, D. G. Vaughan, M. R. Broeke, and L. Padman. 2012. Antarctic ice-sheet loss driven by basal melting of ice shelves. *Nature*, **484**, 502–505. doi: 10.1038/nature10968.
- Reeh, N., H.H. Thomsen, A.K. Higgins, and A. Weidick. 2001. Sea ice and the stability of north and northeast Greenland floating glaciers. *Annals of Glaciology*, **33**(1), 474–480. doi: 10.3189/172756401781818554.
- Rignot, E., G. Casassa, P. Gogineni, W. Krabill, A. Rivera, and R. Thomas. 2004. Accelerated ice discharge from the Antarctic Peninsula following the collapse of Larsen B ice shelf. *Geophysical Research Letters*, **31**(18). doi: 10.1029/2004GL020697.
- Rignot, E., J. L. Bamber, M. R. Broeke, C. Davis, Y. Li, W. J. Berg, and E. Meijgaard. 2008. Recent Antarctic ice mass loss from radar interferometry and regional climate modeling. *Nature Geoscience*, **1**, 106–110. doi:10.1038/ngeo102.
- Rignot, E., J. Mouginot, and B. Scheuchl. 2011. Ice Flow of the Antarctic Ice Sheet.

- Science*, **333**(6048), 1427–1430. doi: 10.1126/science.1208336.
- Sada, T. 2003. *GPS positioning technique*. Ohm-Sha.
- Sawagaki, T., H. Miura, and S. Iwasaki. 2008. Discovery of an ice cave in the Yatude Valley, Langhovde, Dronning Maud Land, East Antarctica. *Polar Science*, **2**, 287–294. doi: 10.1016/j.polar.2008.10.002.
- Scambos, T. A., J. A. Bohlander, C. A. Shuman, and P. Skvarca. 2004. Glacier acceleration and thinning after ice shelf collapse in the Larsen B embayment, Antarctica. *Geophysical Research Letters*, **31**(18). doi: 10.1029/2004GL020670.
- Scambos, T. A., T. M. Haran, M. A. Fahnestock, T. H. Painter, and J. Bohlander. 2007. MODIS-based Mosaic of Antarctica (MOA) data sets: Continent-wide surface morphology and snow grain size. *Remote Sensing of the Environment*, **111**(2–3), 242–257. doi: 10.1016/j.rse.2006.12.020.
- Scherler, D., S. Lepeince, and M.R. Strecker. 2008. Glacier–surface velocities in alpine terrain from optical satellite imagery—Accuracy improvement and quality assessment. *Remote Sensing of Environment*, **112**(2008), 3806–3819. doi: 10.1016/j.rse.2008.05.018.
- Scott, J. B. T., G. H. Gudmundsson, A. M. Smith, R. G. Bingham, H. D. Pritchard, and D. G. Vaughan. 2009. Increased rate of acceleration on Pine Island Glacier strongly coupled to changes in gravitational driving stress. *The Cryosphere*, **3**, 125–131. doi: 10.5194/tc-3-125-2009.
- Shepherd, A., D. J. Wingham, J. A. D. Mansley, and H. F. J. Corr. 2001. Inland thinning of Pine Island Glacier, West Antarctica. *Science*, **291**, 862–864. doi: 10.1126/science.291.5505.862.
- Shuman, C. A., E. Berthier, and T. A. Scambos. 2011. 2001–2009 elevation and mass losses in the Larsen A and B embayments, Antarctic Peninsula. *Journal of Glaciology*, **57**(204), 737–753. doi: 10.3189/002214311797409811.
- Stearns, L. A., B. E. Smith, and G. S. Hamilton. 2008. Increased flow speed on a large

- East Antarctic outlet glacier caused by subglacial floods. *Nature Geoscience*, **1**, 827–831. doi: 10.1038/ngeo356.
- Sugiyama, S., S. Tsutaki, D. Nishimura, H. Blatter, A. Bauder and M. Funk. 2008. Hot water drilling and glaciological observations at the terminal part of Rhonegletscher, Switzerland in 2007. *Bulletin of Glaciological Research*, **26**, 41–47.
- Sugiyama, S., A. Bauder, M. Huss, P. Riesen, and M. Funk. 2008. Triggering and drainage mechanisms of the 2004 glacier-dammed lake outburst in Gornergletscher, Switzerland. *Journal of Geophysical Research*, **113**, F4019. doi: 10.1029/2007JF000920.
- Sugiyama, S., P. Skvarca, N. Naito, K. Tone, H. Enomoto, K. Shinbori, S. Marinsek and M. Aniya. 2010. Hot-water drilling at Glaciar Perito Moreno, Southern Patagonia Icefield. *Bulletin of Glaciological Research*, **29**, 27–32.
- Sugiyama, S., P. Skvarca, N. Naito, H. Enomoto, S. Tsutaki, K. Tone, S. Marinsek and M. Aniya. 2011. Ice speed of a calving glacier modulated by small fluctuations in basal water pressure. *Nature Geoscience*, **4**, 597–600. doi: 10.1038/ngeo1218.
- Sugiyama, S., T. Sawagaki, T. Fukuda, and S. Aoki. 2013. Warm water and life beneath the grounding zone of an Antarctic outlet glacier. *Proceedings of EGU General Assembly 2013, in Vienna, Austria*.
- Tobita, M., M. Murakami, H. Nakagawa, H. Yarai, S. Fujiwara, and P.A. Rosen. 2001. 3-D surface deformation of the 2000 Usu eruption measured by matching of SAR images. *Geophysical Research Letters*, **28**(22), 4291–4294. doi: 10.1029/2001GL013329.
- Toutin, T. 2002. Three-dimensional topographic mapping with ASTER stereo data in rugged topography. *Institute of Electrical and Electronics Engineers (IEEE) Transaction of Geoscience and Remote Sensing*, **40**(10), 2241–2247. doi: 10.1109/TGRS.2002.802878.

- Tsutaki, S., and S. Sugiyama. 2009. Development of a hot water drilling system for subglacial and englacial measurements. *Bulletin of Glaciological Research*, **27**, 7–14.
- Tsutaki, S., D. Nishimura, T. Yoshizawa and S. Sugiyama. 2011. Changes in glacier dynamics under the influence of proglacial lake formation in Rhonegletscher, Switzerland. *Annals of Glaciology*, **52**(58), 31–36. doi: 10.3189/172756411797252194.
- Tsutaki, S., S. Sugiyama, D. Nishimura and M. Funk. 2013. Acceleration and flotation of a glacier terminus during formation of a proglacial lake in Rhonegletscher, Switzerland. *Journal of Glaciology*, **59**(215), 559–570. doi: 10.3189/2013JoG12J107.
- UNESCO. 1981. Background papers and supporting data on the International Equation of State of Seawater 1980. *UNESCO Technical papers in marine science*, **38**, 25.
- Ushio S., and T. Takizawa. 1993. Oceanographic data in Lützow-Holm Bay of Antarctic climate research programme from March 1990 to January 1991 (JARE-31). *JARE Data Reports, Oceanography*, **13**, 1–34.
- Ushio, S. 2006. Factors affecting fast-ice break-up frequency in Lützow-Holm Bay, Antarctica. *Annals of Glaciology*, **44**, 177–182. doi: 10.3189/172756406781811835.
- Ushio, S. 2010. Land-fast ice variation in Lützow-Holm Bay, Antarctica, during the past eight decades. *Summaries of JSSI & JSSE Joint Conference on Snow and Ice Reserach- 2010/Sendai*, The Japanese Society of Snow and Ice, 209.
- Ushio, S. 2012. Sea ice condition in Lützow-Holm Bay, Antarctica, in the austral summer of 2011/12 -Analysis of factors affecting difficulty of ice navigation-. *Summaries of JSSI & JSSE Joint Conference on Snow and Ice Reserach- 2012/Fukuyama*, The Japanese Society of Snow and Ice, 172.
- Vaughan, D. G. 1995. Tidal flexure at ice shelf margins. *Journal of Geophysical*

- Research: Solid Earth*, **100**(B4), 6213–6224. doi: 10.1029/94JB02467.
- Velicogna, I. 2009. Increasing rates of ice mass loss from the Greenland and Antarctic ice sheets revealed by GRACE. *Geophysical Research Letters*, **36**(19), L19503. doi: 10.1029/2009GL040222.
- Vickers, R. S., and R. L. Bollen. 1974. An Experiment in the Radio Echo Sounding of Temperate Glaciers. Final Report, Contract 14-08-000114650 for U.S. Geological Survey, Denver, Stanford Research Institute, Menlo Park, California (October 1974).
- Warrick, R. A., C. L. Provost, M. F. Meier, J. Oerlemans, and P. L. Woodworth. 1996. *Climate Change 1995 The Science of Climate Change, Changes in sea level*, 359–405.
- Wingham, D. J., D. W. Wallis, and A. Shepherd. 2009. The spatial and temporal evolution of Pine Island Glacier thinning, 1995–2006. *Geophysical Research Letters*, **36**(17), L17501. doi: 10.1029/2009GL039126.
- Yu, J., H. Liu, K. C. Jezek, R. C. Warner, and J. Wen. 2010. Analysis of velocity field, mass balance, and basal melt of the Lambert Glacier - Amery Ice Shelf system by incorporating Radarsat SAR interferometry and ICESat laser altimetry measurements. *Journal of Geophysical Research - Solid Earth*, **115**(B11). doi: 10.1029/2010JB007456.

